BULLETIN OF THE POLISH ACADEMY OF SCIENCES
TECHNICAL SCIENCES, Vol. 70(2), 2022, Article number: e140534
DOI: 10.24425/bpasts.2022.140534



# Review of photodetectors characterization methods

**Zbigniew BIELECKI**[1]*, **Krzysztof ACHTENBERG**[1], **Małgorzata KOPYTKO**[2]
**Janusz MIKOŁAJCZYK**[1], **Jacek WOJTAS**[1], and **Antoni ROGALSKI**[2]

[1] Institute of Optoelectronics, Military University of Technology, 2 Kaliskiego Str., 00-908 Warsaw, Poland
[2] Institute of Applied Physics, Military University of Technology, 2 Kaliskiego Str., 00-908 Warsaw, Poland

**Abstract.** The review includes results of analyses and research aimed at standardizing the concepts and measurement procedures associated with photodetector parameters. Photodetectors are key components that ensure the conversion of incoming optical radiation into an electrical signal in a wide variety of sophisticated optoelectronic systems and everyday devices, such as smartwatches and systems that measure the composition of the Martian atmosphere. Semiconductor detectors are presented, and they play a major role due to their excellent optical and electrical parameters as well as physical parameters, stability, and long mean time to failure. As their performance depends on the manufacturing technology and internal architecture, different types of photodetectors are described first. The following parts of the article concern metrological aspects related to their characterization. All the basic parameters have been defined, which are useful both for their users and their developers. This allows for the verification of photodetectors' workmanship quality, the capabilities of a given technology, and, above all, suitability for a specific application and the performance of the final optoelectronic system. Experimentally validated meteorological models and equivalent diagrams, which are necessary for the correct analysis of parameter measurements, are also presented. The current state of knowledge presented in recognized scientific papers and the results of the authors' works are described as well.

**Key words:** photodetectors, detector parameters, photodetector characteristics, measurements of detector parameters.

## 1. INTRODUCTION

The operation of most optoelectronic systems depends mainly on photodetector performance. The photodetector converts the optical signal into an electrical one. It is also the main front-end component of an optical receiver. Many applications require that they should be very fast and offer the best signal-to-noise ratio. Therefore, it should be characterized by low dark current and noise, high quantum efficiency, high responsivity and short response time.

Additionally, in practical applications, emphasis is placed on their low power consumption, low weight, small size, low manufacturing costs (so-called SWaP-C optimization), high durability, operational reliability and long lifetime. The parameters depend mainly on the semiconductor and its architecture. The approximate chronology of photodetector architecture development is as follows [1]:

1) extrinsic photoconductors,
2) intrinsic photoconductors,
3) Schottky barrier photodiodes,
4) metal-insulator-semiconductor (MIS) photodiodes,
5) p–n photodiodes,
6) avalanche photodiodes (APDs),
7) PIN photodiodes,
8) barrier layer photoconductors.

Recently, interfacial work function internal photoemission detectors, superlattice, quantum well and quantum dot detectors, which, due to the principle of operation, are classified as extrinsic photoconductors, have been developed to operate in different spectral bands [2]. In particular, the short time constant of semiconductor detectors with quantum wells and quantum dots makes them attractive for heterodyne detection. Different basic types of detectors have been listed and described in Table 1.

Measurement of detector parameters is a complex issue due to the large number of experimental variables that need to be considered. Different electrical and radiometric parameters must be precisely and simultaneously controlled. With the increasing use of large, two-dimensional detector arrays, detectors characterization has become even more complex and demanding. In this paper, we will first define the basic parameters of photon detectors and then discuss the basic measuring systems for their characterization.

## 2. DETECTOR PARAMETERS

In this section, the basic parameters of photodetectors will be defined.

### 2.1. Detector signal

The detector signal is usually the voltage or current value that appears at the detector output due to incident radiation. The signal value depends on detector bias voltage $V_b$, modulation frequency $f$, wavelength $\lambda$, radiant flux $\Phi_e$, the detector's active area $A_d$ and temperature $T$.

$$V_s = V_s(V_b, f, \lambda, \Phi_e, A_d, T),$$
$$I_s = I_s(V_b, f, \lambda, \Phi_e, A_d, T). \quad (1)$$

*e-mail: zbigniew.bielecki@wat.edu.pl

Manuscript submitted 2021-09-21, revised 2022-01-18, initially accepted for publication 2022-01-19, published in April 2022.

**Table 1**
Photon detectors

| Operation and properties | Structure of detector | Schematic energy band diagram |
|---|---|---|
| **Photoconductive detectors** use the increase in electrical conductivity resulting from photogeneration of free carriers. They can be divided into intrinsic and extrinsic ones. Intrinsic photoconductive detectors utilize a photon's absorption with sufficient energy to create electron-hole (e-h) pairs in a semiconductor. The spectral response, in this case, is determined primarily by the semiconductor bandgap. An extrinsic photoconductor depends upon the ionization of impurities in the semiconductor, and in this case, only one carrier type, either electrons or holes, is active. The ionization energy of impurities determines the extrinsic spectral response. A similar situation is true for a quantum-well photoconductor, in which electrons or holes can be photoexcited from a potential well in the conduction or valence bands of the semiconductor. | 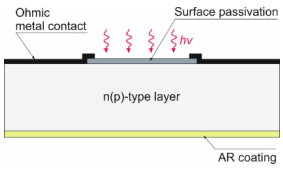 | 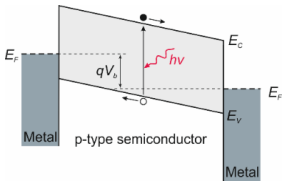 |
| **A p–n junction photodiode** is a widely used optical detector. The device with a p on n configuration consists of a shallow diffused p-region to the n-type active layer. When photons with energy greater than the semiconductor bandgap fall on the neutral regions on both sides of the junction, they create e-h pairs. Then, the carriers generated within the diffusion length from the junction reach the space charge region by means of diffusion, and there they are separated by an electric field (minority carriers become majority carriers on the other side). A photocurrent is generated this way, and it causes a voltage change across the open-circuit cell or a current flow in the short-circuited case. | 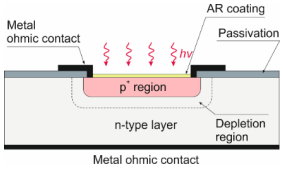 | 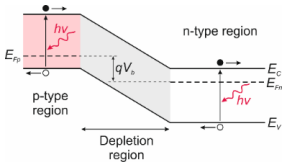 |
| **A Schottky barrier photodiode** is a majority carrier device formed at a metal-semiconductor (m-s) junction. Similarly to the p–n junction, the m-s interface provides a potential barrier that separates the optically generated e-h pairs. The generation of carriers can take place both in the neutral semiconductor region and in the space charge region at the m-s interface. Compared to the p–n junction photodiode, the Schottky barrier reveals some advantages: simplicity of fabrication (deposition of a metal barrier on an n or p semiconductor), no high-temperature diffusion processes, and high response speed. They also have a relatively high dark current. | 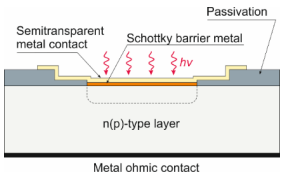 | 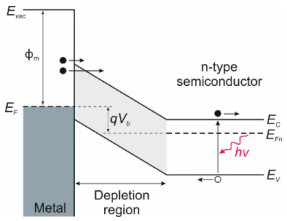 |
| **A metal-insulator-semiconductor (MIS) photodiode** consists of an insulator to separate a metal gate from a semiconductor surface. In this type of photodiode design, the key issue is the appropriate thickness of the insulation layer, which cannot drop below roughly 10 nm. With thinner insulating layers, quantum electron tunneling through this layer may occur. By applying negative voltage to the metal electrode, the electrons are repelled from the insulator-semiconductor interface, creating a depletion region. The total charge that can be collected on the photogate is referred to as its well capacity. This capacitance depends on gate polarization, insulator thickness, electrode surface and background doping of the semiconductor. | 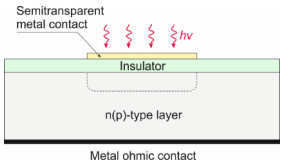 | 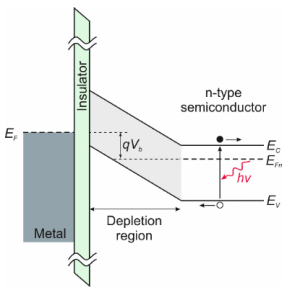 |
| **An avalanche photodiode (APD)** can detect a weak optical signal due to the avalanche multiplication of carriers. The reverse bias applied to the device should be large enough for the depletion layer to extend throughout the n-region. Photon absorption occurs in the p-region. When photogenerated minority carriers (e.g. electrons) reach the edge of the depleted region, they are accelerated under the electric field and gain enough energy to start multiplication. APD offers a combination of high speed, high sensitivity and high quantum efficiency. | 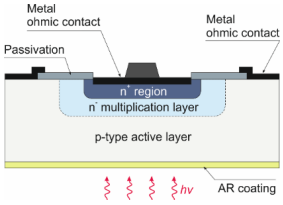 | 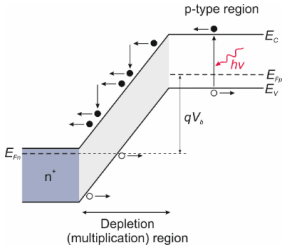 |

**Table 1** [cont.]
Photon detectors

| Operation and properties | Structure of detector | Schematic energy band diagram |
|---|---|---|
| **A PIN photodiode** is a standard photodiode in which an intrinsic region (absorber) is between the p-type and n-type, typically heavily doped regions necessary for ohmic contacts. Under an appropriate reverse bias, the depletion region occupies the entire intrinsic volume defined by the absorber doping-thickness product. When p- and n- regions have a higher energy gap, the incident photons are absorbed only in the depletion region, where e-h pairs are created. The lack of electrically neutral volume causes no diffusion current in the device. Furthermore, the dark current results only from minority carriers generated through the defect centers located in the diode depletion region. Diffusion dark current is also generated in the neutral p- and n-type regions, but in the case of an extended energy gap, it may be negligible. | 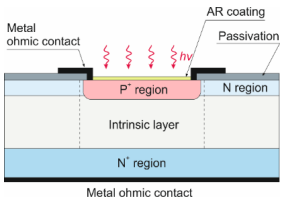 | 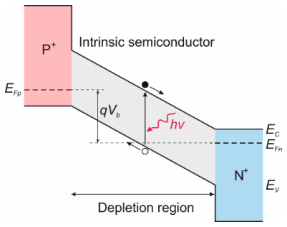 |
| **A barrier layer detector** is a hybrid of a photodiode and a photoconductor. The nBn detector looks in part like the n-p photodiode, except for one major difference that determines the device operation: the space charge region is replaced by a unipolar electron-blocking barrier (B), while the flow of optically generated holes is unimpeded. Therefore, key issue is the zero offset in the valence band across the heterostructure. The type of doping of the upper contact does not significantly influence the operation of the device: it can be of both of the p- or n-type, the latter being used when the same type of doping is easier to obtain. A unipolar barrier is introduced to suppress dark current and noises without impeding photocurrent flow. Moreover, the use of an upper n-type contact with a wide-gap barrier blocks the surface leakage current [3]. | 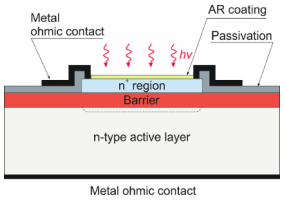 | 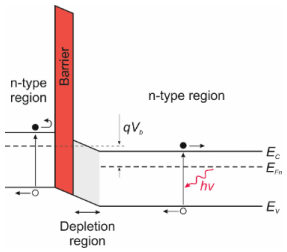 |

The detector signal is a linear function of the radiant flux with less than a limit value power for most detectors. Since only such detectors are considered in this review, the $V/\Phi_e A_d$ ratio is fixed at certain $V_b$, $f$ and $\lambda$. In many cases, the signal dependence on $f$ and $\lambda$ can be separated.

### 2.2. Radiation power

Correctly defining the detector's parameter is necessary to know the incident radiation power (also called radiant flux) and its spectral and spatial distribution. The radiant flux is the energy of source radiation per unit of time defined by:

$$\Phi_e = \frac{\mathrm{d}Q_e}{\mathrm{d}t}. \tag{2}$$

The unit of radiant flux is the watt (W = J/s).

Usually, the modulated radiant flux falls on the detector. Since the modulation can be performed in various ways (e.g. rectangular), it is assumed that the radiant flux of the fundamental component of the Fourier development of the modulation course is given [4]. The modulation frequency is the fundamental frequency. Rectangular modulation is commonly used in the measurements of detector parameters.

For testing infrared detectors, blackbodies simulators of 500 K are commonly used. A perfect blackbody has a precisely defined characteristic of the spectral distribution of the radiation power [5].

### 2.3. Active area

A photodetector's active area is usually the physical region that converts incoming optical radiation into an electric output signal. The diameter is usually given for detectors with a circular surface, whereas for detectors with a rectangular and square surface, its length and width are provided.

### 2.4. Optical area

The apparent active area of the optically immersed detector may differ from the physical active area due to optical concentrators. The optical detector area can be significantly magnified in detectors supplied with optical concentrators, i.e. immersion lenses (Fig. 1).

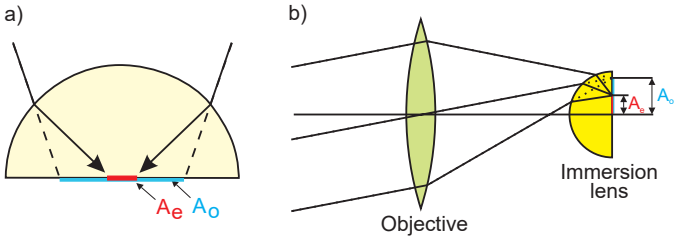


**Fig. 1.** Rays propagation in optical immersion (a), and beam tracing for an optical system with a combination of an objective lens and an immersion lens (b) [6]. $A_e$ and $A_o$ are the electrical active and the photodetector optical active areas, respectively. The use of an optical concentrator can increase the $A_o/A_e$ ratio by a large factor

### 2.5. Bias voltage

Many detectors require a low noise DC voltage supply. The detector output signal and noise are a function of both the bias and radiation modulation frequency. The bias should provide the conditions for a maximum signal-to-noise ratio.

### 2.6. Breakdown voltage

Breakdown voltage is the maximum reverse voltage that can be applied to a detector without the risk of its damage. Beyond breakdown voltage, the photodiode readily conducts the current, so current-limiting protection is also necessary to use.

### 2.7. Photocurrent

The photocurrent is a current generated by a photodetector under the influence of optical radiation. For a small radiation signal, the photocurrent is proportional to the incident radiation power:

$$I_{ph} = q\eta A\Phi_e g\,, \tag{3}$$

where $q$ – elementary charge, $\eta$ is the quantum efficiency, and $g$ is the photoelectric current gain. In general, the photoelectric current gain in a typical photovoltaic detector is equal to unity (it can be much more significant, for example, in an avalanche photodiode).

### 2.8. Photoelectric current gain

Figure 2 shows the successive phases of this phenomenon, the so-called photorecycling effect. After the electron and hole pair generation, the electron reaches the positively charged electrode much faster than the hole reaches the negative electrode and leaves the sample quickly. However, to maintain electrical neutrality of the sample, another electron must enter the sample from the negative electrode as in (b) (the electrode is ohmic). This new electron also quickly reaches the electrode as in (b) and (c), and leaves the sample while the hole is still drifting slowly through the sample. Thus, another electron must enter the sample to maintain neutrality as in (d) and (e), and so on, until either the hole reaches the negative electrode or recombines with one of these electrons entering the sample. Therefore, the resulting photocurrent corresponds to the flow of many electrons onto the absorbed one photon, which represents the photoconductive gain (PC). In intrinsic photoconductors, the measured photoconductivity gain reaches the value of $10^6$. Large PC values are achievable only in the short wavelength infrared (SWIR) or for cryogenically cooled devices. The gain is even $< 1$ for longer wavelengths devices operating near room temperature.

The photoconductive phenomenon is a particular example of photogating, which can be realized in two different ways:

- generation of electron-hole (e-h) pairs, when the localized states (nano-particles and defects) trap one type of charge carrier, and
- generation of e-h pairs in trap-states with one type of charge carrier being transferred, e.g. to two-dimensional (2D) materials, while the other resides at the same place to modulate the layered materials.

In both cases, sensitivity enhancement comes at the cost of photoresponse speed due to a long carrier lifetime.

The simple architecture of the second solution, the so-called hybrid phototransistor, is shown in Fig. 3. It is very popular in designing photodetectors with a fast transfer channel for charge carriers, particularly with 2D materials. Since in these devices the 2D material, e.g. graphene, is not responsible for the absorption of light but only for the charge sensing, the choice of the absorber material determines the spectral range of the device's operation. The large ambipolar mobility of graphene acts as a built-in photogain (i.e. amplifier) mechanism enhancing detector responsivity. Atomic layer thickness 2D materials are more susceptible to local electric fields than conventional bulk materials, and the photogating effect can strongly modulate channel conductivity by means of external gate voltage, $V_G$. This way, ultra-high gain of up to $10^8$ electrons per photon and exceptional responsivities for short-wavelength infrared photodetectors have been demonstrated [7].

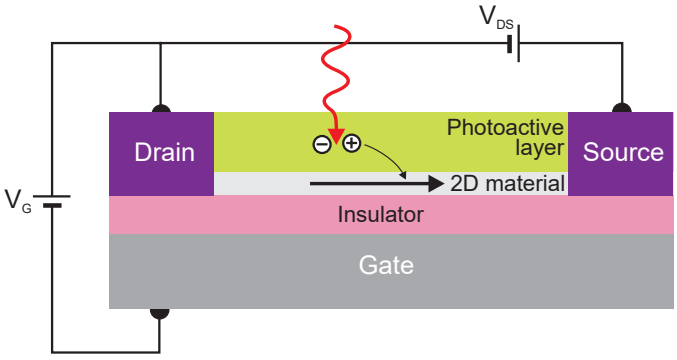


**Fig. 3.** Operation of hybrid phototransistor

### 2.9. Dark current-voltage (I-V) equation

Dark current-voltage (I-V) equation describes the operation of a photodiode without incident light. When the photodiode is reverse biased, a small saturation current, $I_s$, flows in the circuit.

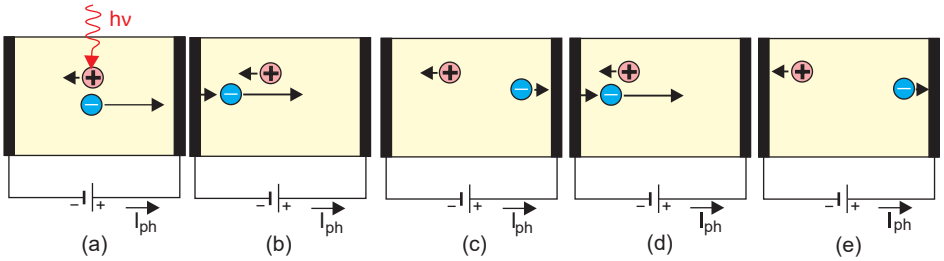


**Fig. 2.** The idea of photoconductivity enhancement in a photoconductor

When a forward bias is applied, the current increases exponentially. It is related to dark current as:

$$I_d = I_s \left[ \exp\left( \frac{qV}{\beta kT} \right) - 1 \right], \tag{4}$$

where, $q$ is the electron charge, $\beta$ is the ideality factor of the junction, $k$ is the Boltzmann constant and $T$ is temperature.

### 2.10. Saturation current

Saturation current $I_s$ is an electric current that flows through the reverse-biased photodiode even when no radiation illuminates the device. Physically, the saturation current is due to the thermal generation of e-h pairs within the diffusion and depletion region of the photodiode. There are three primarily generation-recombination (g-r) mechanisms in direct-bandgap semiconductors: radiative, Auger and Shockley–Read–Hall (SRH). The two first are fundamental mechanisms determined by the semiconductor's band structure and doping concentration, whereas defects or impurities determine SRH. The saturation current depends exponentially on the absorber bandgap and temperature. It is low for the short cutoff wavelength devices but is significant for long-wavelength infrared (LWIR) devices.

### 2.11. Diffusion current

Diffusion current arises from the thermal generation of carriers in the un-depleted (electrically neutral) semiconductor within a minority carrier diffusion length. The diffusion current dependent on the radiative, Auger and SRH generation can be described as follows:

$$I_{\text{dif}} = \frac{Aqn_i^2 t}{N_{\text{maj}}} \left( \frac{1}{\tau_R} + \frac{1}{\tau_A} + \frac{1}{\tau_{\text{SRH}}} \right), \tag{5}$$

where $n_i$ is the intrinsic carrier concentration, $t$ is the thickness of the electrically neutral region, $N_{\text{maj}}$ is the appropriate majority carrier concentration (electron concentration for the n-type material and hole concentration for the p-type material), $\tau_R$ is the lifetime due to radiative recombination [8], $\tau_A$ is the lifetime due to Auger recombination [9], and $\tau_{\text{SRH}}$ is the lifetime for recombination through defect centers in the bandgap [10–12]. For n-type semiconductors, the Auger 1 effect is the primary mechanism due to the interaction of two electrons and one hole. In p-type material, the primary Auger recombination mechanism involves two holes and one electron, and is referred to as Auger 7.

### 2.12. Depletion current

Depletion current arises from the portion of the semiconductor that becomes depleted. The depletion current can be estimated by:

$$I_{\text{dep}} = \frac{Aqn_i W}{\tau_{\text{SRH}}}, \tag{6}$$

where $W$ is the width of the depletion region, expressed as [13]:

$$W = \left[ \frac{2\varepsilon\varepsilon_0 (V_{bi} - V)}{qN_{\text{maj}}} \right]^{1/2}, \tag{7}$$

for a one-side abrupt junction, and:

$$W = \left[ \frac{2\varepsilon\varepsilon_0}{q} \left( \frac{N_a + N_d}{N_a N_d} \right) (V_{bi} - V) \right]^{1/2}, \tag{8}$$

for a sided-side abrupt junction, where $\varepsilon$ is the dielectric constant, $\varepsilon_0$ is the vacuum permittivity and $V_{bi}$ is the built-in potential. For the reverse-biased photodiode $V = -V_b$, and for the forward-biased photodiode $V = +V_b$. $N_a$ is the acceptor carrier concentration in the p-type region, and $N_d$ is the donor carrier concentration in the n-type region of the junction.

Operation mode. A photodiode can operate in either the photovoltaic or photoconductive mode. In the photovoltaic mode, the photodiode is unbiased ($V_b = 0$). An external reverse bias is applied for the photoconductive mode [14]. As shown in Fig. 4, an illumination of the photodiode with optical radiation shifts the current-voltage curve by the amount of photocurrent. The operation mode selection depends upon the performance requirements of the application. The detectors optimized for low or moderate frequencies operate under zero bias voltage

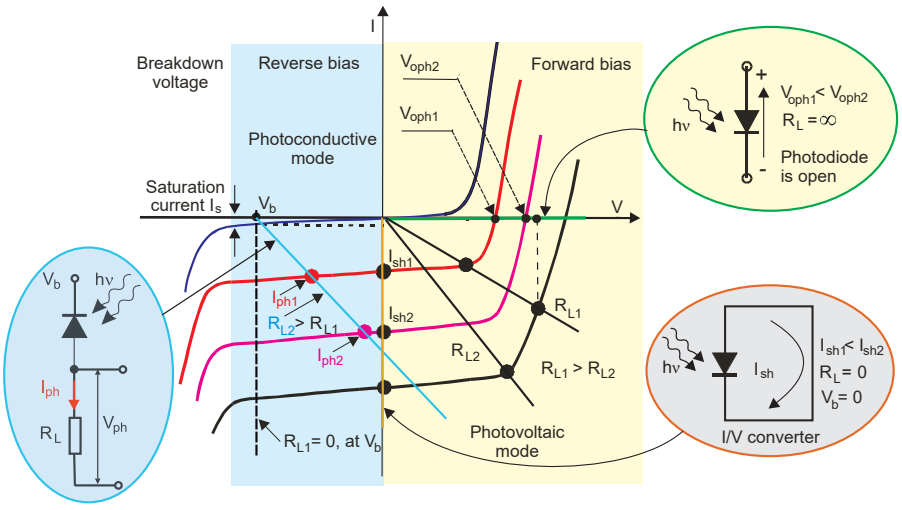


**Fig. 4.** Current–voltage characteristics of a photodiode for a photovoltaic and photoconductive mode of operation

and current mode conditions. Constant reverse bias and current readout are used for high-frequency (HF) operation. These operation modes are typically achieved with transimpedance preamplifiers.

Figure 4 shows load lines for photodiode operation in a photovoltaic and photoconductive mode. It results from the intersection of the load line with the *I–V* characteristics. If the photodiode works in a photovoltaic circuit, the load line passes through the origin of the coordinate system and intersects the photodiode characteristics in the fourth quadrant of the coordinate system. When $R_L = \infty$, the load line coincides with the abscissa axis. It is possible to read the voltage $V_{\text{oph}}$. The voltage at which the *I–V* characteristic crosses the abscissa is called the open-circuit voltage $V_{\text{oph}}$. It changes logarithmically with a change of the incident radiation power.

The photodiode operating point for lower load resistance values is determined by voltage $V_{ph}$ and photocurrent $I_{ph}$. In this case, it is possible to measure both voltage $V_{ph}$ and current $I_{ph}$. The value of resistance $R_L$, for which the product $V_{ph}$, $I_{ph}$ takes the maximum value, should be treated as optimal resistance $R_{L\text{opt}}$.

Other effects commonly observed in a photodiode are parasitic resistive effects, which reduce the device's efficiency by the current, owing to shunt resistance $R_{sh}$ and series resistance $R_s$ (see Fig. 5).

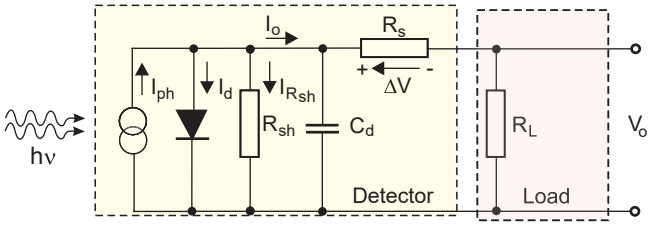


**Fig. 5.** Equivalent small-signal circuit of a photodiode (where $I_d$ – diode current, $I_{\text{Rsh}}$ – shunt resistance current, $I_o$ – output current)

### 2.13. Shunt resistance

In parallel to the photodiode, the resistor is called the shunt resistance, $R_{sh}$. It originates in imperfections of the p–n junction and allows for a certain amount of leakage around junction edges or/and through defects or impurity phases. An ideal photodiode will have an infinite shunt resistance and will not provide an alternate path for the current flow. With infinite or extremely high shunt resistance, a current source delivers all its currents to the load. The current-to-voltage conversion is determined entirely by the load resistance, $R_L$. $R_{sh}$ may range from hundreds to thousands of megaohms for silicon photodiodes, and indium gallium arsenide can also have extremely high shunt resistance. Shunt resistance also influences noise performance. As $R_{sh}$ decreases, both photodiode's Johnson noise current and $1/f$ noise current increase.

### 2.14. Series resistance

Series resistance, $R_s$, of a photodiode results from contact resistance, wire bonds and non-depleted quasi-neutral material. For an ideal photodiode, the value of the series resistance is equal to zero, whereas for a real photodiode, depending on the spectral range, it can be from several to several hundred ohms. The current passing through $R_s$ creates voltage drop $\Delta V$ that reduces the bias across the depletion region.

### 2.15. Photodiode impedance

Photodiode consists of depletion (built-in electric field) and diffusion (field-free) regions connected in series. These regions provide a parallel connection of a capacitor and a resistor, as shown in Fig. 6. $C_{\text{dep}}$ and $R_{\text{dep}}$ mean capacitance and resistance of the depletion region, respectively, while $C_{\text{dif}}$ and $R_{\text{dif}}$ mean capacitance and resistance of the diffusion region, respectively. In the equivalent model, $C_{pd}$ and $R_{pd}$ mean the total capacitance and resistance of the photodiode, respectively. They can be used to express impedance of the small signal of the junction photodiode:

$$Z = \left( \frac{1}{R_{pd}} + j\omega C_{pd} \right)^{-1}, \tag{9}$$

where $\omega = 2\pi f$.

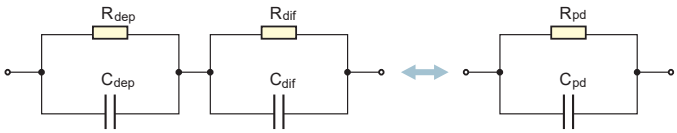


**Fig. 6.** Equivalent model for calculation of photodiode resistance and capacitance

Junction capacitance is directly proportional to a photodiode's active area and can be reduced by reverse biasing.

Diffusion capacitance, due to the excess carrier stored, comes from the rearrangement of minority carrier density [15]. When the junction is forward-biased, it consists of a significant contribution to diode capacitance. Typically, in a forward biased diode, diffusion capacitance is distinctly larger than junction capacitance. In general, $C_{\text{dif}}$ and $R_{\text{dif}}$ determine the cut-off frequency of the photodiode, where diode capacitance falls from $C_{\text{dep}}$ to $C_{\text{dep}} \cdot C_{\text{dif}}/(C_{\text{dep}} + C_{\text{dif}})$.

### 2.16. Dynamic resistance

Dynamic resistance (also called *differential* or *incremental* resistance) is the ratio of a small change in voltage to the resulting small change in the current. It is defined as the inverse slope of the *I–V* curve at $V = V_b$

$$R_d = \left( \frac{\delta I}{\delta V} \right)^{-1}_{V=V_b}. \tag{10}$$

### 2.17. Resistance-area product

Area-normalized dynamic resistance of photodiodes that is used to compare photodiodes of different dimensions in which dynamic resistance decreases proportionally to the active detector area:

$$R_d A_d = \left( \frac{\delta J}{\delta V} \right)^{-1}_{V=V_b}, \tag{11}$$

where $J$ is the current density ($J = I/A_a$).

### 2.18. $R_0A$ product

The product of $R_0A$ is a frequently encountered figure of merit for a photodiode operated at a zero-bias voltage ($V_b = 0$), where $R_0$ is photodiode resistance at zero-bias voltage.

$$R_0A = \left(\frac{\delta J}{\delta V}\right)^{-1}_{V_b=0}. \tag{12}$$

### 2.19. Short-circuit current

Short-circuit current ($I_{sh}$) is the current generated by a photodiode into a short circuit when the diode is illuminated. $I_{sh}$ depends on the intensity and spectral distribution of the light source.

### 2.20. Total current

The total current that flows through the illuminated real p–n junction (including parasitic resistances) is expressed as [13, 16]:

$$I_{\text{total}} = I_{ph} - I_{\text{dif}}\left[\exp\left(\frac{q(V+IR_s)}{n_1kT}\right)-1\right] - I_{\text{dep}}\left[\exp\left(\frac{q(V+IR_s)}{n_2kT}\right)-1\right] - \frac{V+IR_s}{R_{sh}}, \tag{13}$$

where $I_{\text{dif}}$ is the diffusion current defined by equation (5), generated within the electrically neutral regions of the diode, $I_{\text{dep}}$ is the current generated within the depletion region of the diode, given by equation (6), and $n_1$ and $n_2$ are their respective ideality factors.

### 2.21. Open-circuit voltage

If the photodiode is open-circuited, the accumulation of electrons and holes on either side of the p–n junction produces an open-circuit voltage, $V_{\text{oph}}$. The short-circuit current, $I_{sh}$, will appear if a load resistance is connected to the diode. Open-circuit voltage is the product of the short-circuit current and the incremental diode resistance at zero bias voltage:

$$V_{\text{oph}} = I_{sh}R_0. \tag{14}$$

### 2.22. Quantum efficiency

Quantum efficiency $\eta$ is usually defined as the number of e-h pairs generated by the photodetector per photons incident on its active area. This parameter is a standardized value, generally less than a unity or expressed as a percentage. This way, we limit the generation of e-h pairs to their creation, eliminating, e.g. avalanche multiplication of the carriers. Deviations from the above definition are observed in the high energy of photons, where quantum efficiency can reach values beyond a unity. Not all absorbed photons may generate free e-h pairs that can be collected. Some carriers may recombine or become immediately trapped. If the thickness of the semiconductor layer in which the absorption takes place is comparable with the penetration depth ($1/\alpha$, where $\alpha$ is the absorption coefficient), not all photons will be absorbed. Quantum efficiency also depends on reflection from the detector surface, absorption coefficient and device structure. It can be increased by reducing the reflections at the semiconductor surface, increasing absorption and preventing the recombination or trapping of carriers. The quantum efficiency of an ideal photodetector is a binary function – the photon energy is enough to excite the medium ($\eta = 100\%$) or is insufficient ($\eta = 0$). Figure 7 shows the quantum efficiency *vs.* the wavelengths for the ideal and real detector.

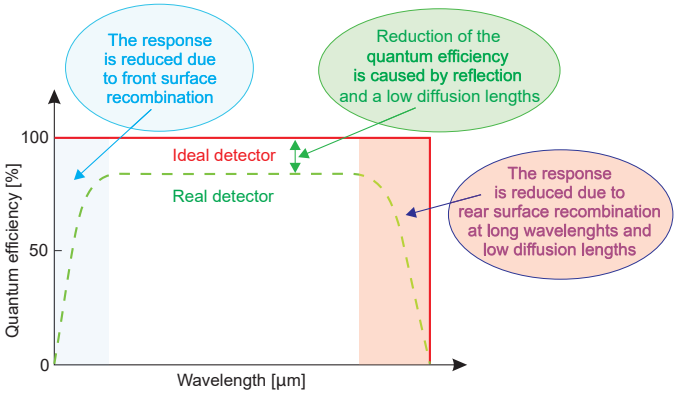


**Fig. 7.** Quantum efficiency vs. wavelengths for ideal and real detector

### 2.23. Responsivity

The detector's responsivity is defined as the ratio of the root mean square (RMS) value of the fundamental component of the detector electrical output signal to the RMS value of the fundamental component of the input radiation power. For example, the current (or analogous voltage) responsivity is determined by the ratio of the photocurrent $I_o$ (photovoltage $V_o$) to the incident light power $\Phi_e$ at a given wavelength, $\lambda$:

$$R_i = \frac{I_o}{\Phi_e}, \quad R_v = \frac{V_o}{\Phi_e}. \tag{15}$$

Generally, responsivity is a measure of how efficiently the power of light is converted into electrical current. The unit of responsivity is either ampere per watt or volts per watt, depending on whether the output is an electric voltage or a current one. Responsivity depends on the semiconductor energy gap, therefore it varies with the wavelength of the incident light (Fig. 8) and temperature (the energy gap varies with temperature). In some cases it may also depend on the reverse bias applied.

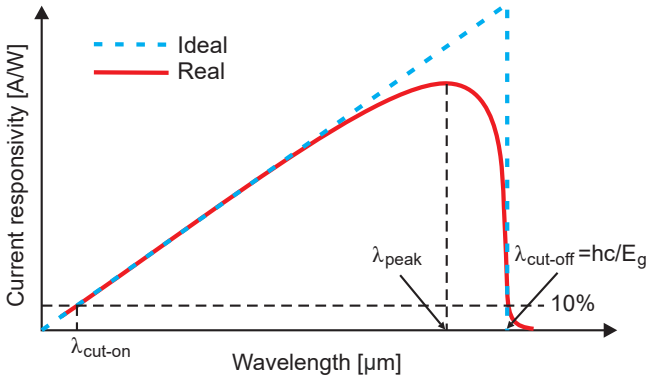


**Fig. 8.** Relative current responsivity of ideal and real photodiodes

### 2.24. Spectral responsivity

It is the dependence of current (or analogous voltage) responsivity on the wavelength, and it is given by:

$$R_i(\lambda, f) = \frac{I_{ph}}{\Phi_e(\lambda)\Delta\lambda}, \qquad R_v(\lambda, f) = \frac{V_{ph}}{\Phi_e(\lambda)\Delta\lambda}, \tag{16}$$

where $\Phi_e(\lambda)$ is the spectral radiant incident power (in W/μm).

### 2.25. Cut-on wavelength

Cut-on wavelength $\lambda_{\text{cut-on}}$ is the shortest wavelength at which detector responsivity reaches 10% of the peak value.

### 2.26. Peak wavelength

Peak wavelength $\lambda_{\text{peak}}$ is a wavelength at which a detector reaches its maximum responsivity.

### 2.27. Cut-off wavelength

Cut-off wavelength $\lambda_{\text{cut-off}}$ is the longest wavelength at which detector responsivity reaches 50% of the peak value.

### 2.28. Response time

In many applications where the signal frequency is being measured or where a fast photoreceiver is required, the rise and fall time of the detector become very important. The rise time of the detector output signal, which is the detector's response to rectangular pulse extortion, is the time required for the photodetector to increase its output from 10% to 90% of the final output level (Fig. 9). The detector's fall time is defined as the time required for the signal to fall from 90% to 10% of the final value. The rise time can also be expressed as frequency response, the frequency $f_c$ at which the photodiode output decreases by 3 dB relative to the 100% output level.

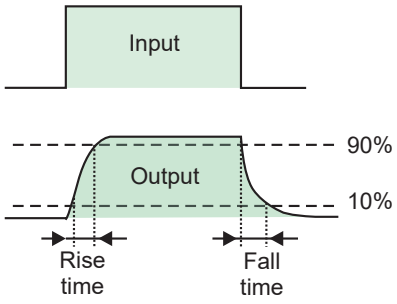


**Fig. 9.** Examples of response waveform

It can be presented by:

$$t_r = \frac{0.35}{f_c}. \tag{17}$$

This expression is valid for detectors having only one time constant. The following equation can approximate the frequency response characteristics of detector responsivity:

$$R_i = \frac{R_{io}}{(1+\omega^2\tau^2)}, \tag{18}$$

where $R_{io}$ is the detector responsivity at zero frequency of the incident radiation modulation and $\tau$ is the time constant of the detector-preamplifier combination response:

$$\tau = (\omega_{-3\,\text{dB}})^{-1}, \tag{19}$$

where $\omega_{-3\,\text{dB}}$ is the angular frequency at which responsivity has fallen to 0.71 of its maximum value (see Fig. 10). In addition, the relation

$$\omega_{-3\,\text{dB}} = 2\pi f_c \tag{20}$$

is occurring. More complex cases are possible when the detector has different recombination mechanisms and several time constants.

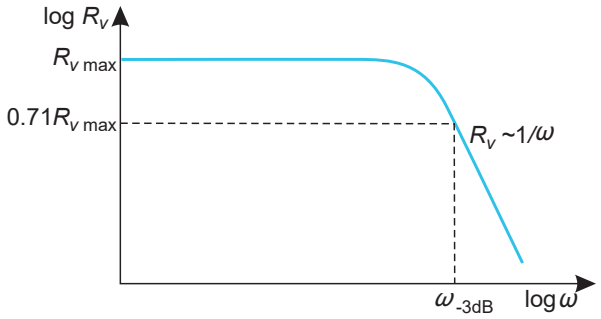


**Fig. 10.** Detector responsivity vs. angular frequency

### 2.29. Noise equivalent power (NEP)

NEP is the incident power on the detector that produces a signal-to-noise ratio (SNR) of unity at the output at a given data-signaling rate or modulation frequency, wavelength and noise bandwidth. NEP can be used to determine spectral sensitivity. In terms of responsivity it can be written as:

$$\text{NEP} = \frac{I_n}{R_i} = \frac{V_n}{R_v}, \tag{21}$$

and is expressed in watt. $I_n$ and $V_n$ are the noise current and noise voltage, respectively.

Since the RMS value of the noise voltage is proportional to the square root of the bandwidth, the NEP is also expressed in the spectral density unit W/Hz$^{1/2}$.

The lowest NEP = NEP$_{\text{min}}$ is obtained for a given detector at the wavelength with maximum detector responsivity. Thus:

$$\text{NEP}(\lambda) = \text{NEP}_{\text{min}}\frac{R_{\text{max}}}{R(\lambda)}, \tag{22}$$

where $R_{\text{max}}$ is the maximum detector responsivity and $R(\lambda)$ is the detector responsivity at wavelength $\lambda$.

The minimum detectable power $P_{\text{min}}$ can be calculated using the following equation:

$$P_{\text{min}} = \text{NEP}(\lambda)\Delta f^{1/2}, \tag{23}$$

where $\Delta f$ is the noise measurement bandwidth.

### 2.30. Shot noise

Shot noise is related to the statistical fluctuation in both the dark current and the photocurrent. When photodiodes operate in photoconductive (biased) mode, shot noise is the dominating source. The magnitude of the shot noise is expressed as the root mean square (RMS) noise current:

$$I_{sn} = \left[2q\left(I_d + I_{ph}\right)\Delta f\right]^{1/2}. \tag{24}$$

### 2.31. Thermal noise

The source of thermal noise (or Johnson noise) is associated with photodetector resistance. This is due to the thermal generation of carriers. The magnitude of this noise current is:

$$I_{jn} = \left[\frac{4kT\Delta f}{R_0}\right]^{1/2}. \tag{25}$$

### 2.32. Total RMS noise current

Total RMS noise current generated in a photodetector is determined by:

$$I_n = \left[I_{sn}^2 + I_{jn}^2 + I_{n\,\text{other}}^2\right]^{1/2}, \tag{26}$$

where $I_{n\,\text{other}}$ – other noises ($1/f$ noise, g-r noise, ...).

### 2.33. Detectivity

Detectivity $D(\lambda)$ is the reciprocal of NEP:

$$D(\lambda) = \frac{1}{\text{NEP}}. \tag{27}$$

Many experimental and theoretical studies have shown that detectivity is inversely proportional to the square root of the active detector area and, therefore:

$$DA_d^{1/2} = \text{const}. \tag{28}$$

Given this, R.C. Jones has introduced the normalized detectivity $D^*$ (or $D$-star) related to the unit detector area and the unit bandwidth [17]. It means that both NEP and $D^*$ are functions of the electrical bandwidth and detector active area:

$$D^* = D\left(A_d\Delta f\right)^{1/2} = \frac{\left(A_d\Delta f\right)^{1/2}}{\text{NEP}}. \tag{29}$$

It is the most crucial detector parameter which allows for comparison of the same type of detectors with different areas (see Fig. 11). $D^*$ is expressed in the unit of cmHz$^{1/2}$/W, which is more commonly called 'Jones' and is defined as the

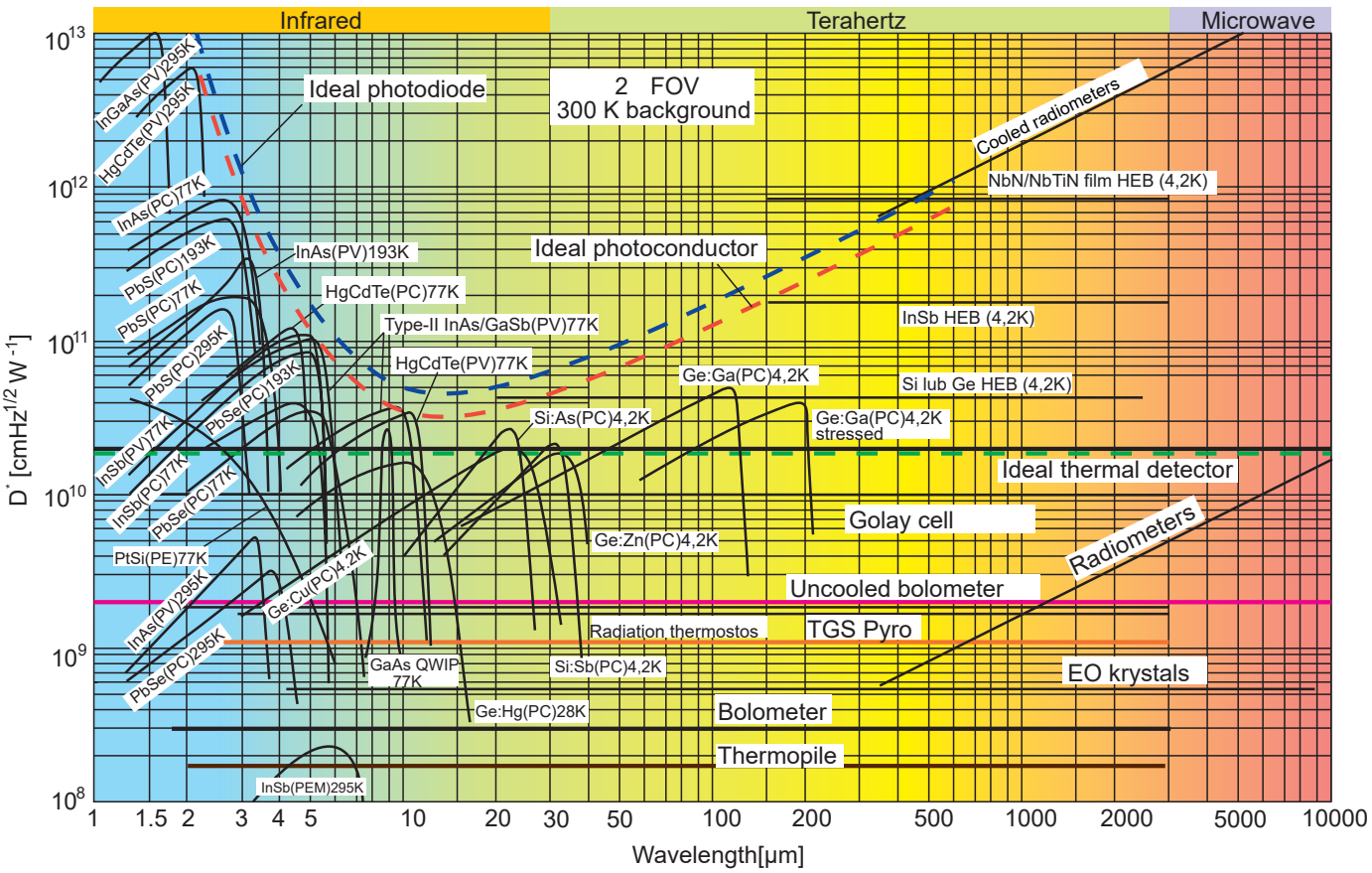


**Fig. 11.** $D^*$ of various available detectors operated at the different temperatures with chopping frequency of 1000 Hz for all detectors except the thermopile, thermocouple, thermistor bolometer, Golay cell, and pyroelectric detector (10 Hz). Each detector is assumed to view a hemispherical surrounding at a temperature of 300 K. Theoretical curves for the background-limited $D^*$ (dashed lines) for some detectors are also shown: PC: photoconductive detector, PV: photovoltaic detector, PEM: photoelectromagnetic detector, and HEB: hot electron bolometer (after [18])

RMS SNR in a 1-Hz bandwidth per unit RMS incident radiation power per square root of detector area:

$$D^* = \frac{(A_d \Delta f)^{1/2}}{I_n} R_i = \frac{(A_d \Delta f)^{1/2}}{V_n} R_v = \frac{(A_d \Delta f)^{1/2}}{\Phi_e} \text{SNR}. \quad (30)$$

The blackbody $D^*(T,f)$ can be determined by knowing spectral detectivity:

$$D^*(T,f) = \frac{\int_0^\infty D^*(\lambda,f)\Phi_e(T,\lambda)\,\mathrm{d}\lambda}{\int_0^\infty \Phi_e(T,\lambda)\,\mathrm{d}\lambda} = \frac{\int_0^\infty D^*(\lambda,f)E_e(T,\lambda)\,\mathrm{d}\lambda}{\int_0^\infty E_e(T,\lambda)\,\mathrm{d}\lambda}, \quad (31)$$

where $\Phi_e(T,\lambda) = E_e(T,\lambda)A$ is the incident blackbody radiant flux (in W) and $E_e(T,\lambda)$ is the blackbody irradiance (in W/cm$^2$).

### 2.34. Background generated current

The ultimate performance of optical detectors is reached when the detector and amplifier noise is low compared to the photon's ones. The radiation falling on the detector is a composite of signals originating from the source and background.

We can distinguish two extreme cases where it is dominant:

- signal photon noise – which means detector performance limited by signal fluctuations,
- background photon noise – which means detector performance determined by background fluctuations (background-limited performance – BLIP).

The detector operating conditions defined by the first case occur relatively rarely at short wavelengths (ultraviolet and visible range), e.g. in photomultipliers. However, they are not registered for semiconductor detectors, the performance of which is determined by the self-noise or the noise of the read-out electronics.

Figure 12 is a curve showing how ideal $D^*_{BLIP}$ is improved as the cone angle $\theta$ is reduced for any given background temperature [19]. In this figure, the detector's field of view (FOV) angle is also marked with the symbol $f/\#$. It denotes the system focal length ratio to the diameter of the entrance pupil $d$ called the $f$-number (e.g. $f/1$ means $f/d = 1$; and $f/2$ means $f/d = 2$).

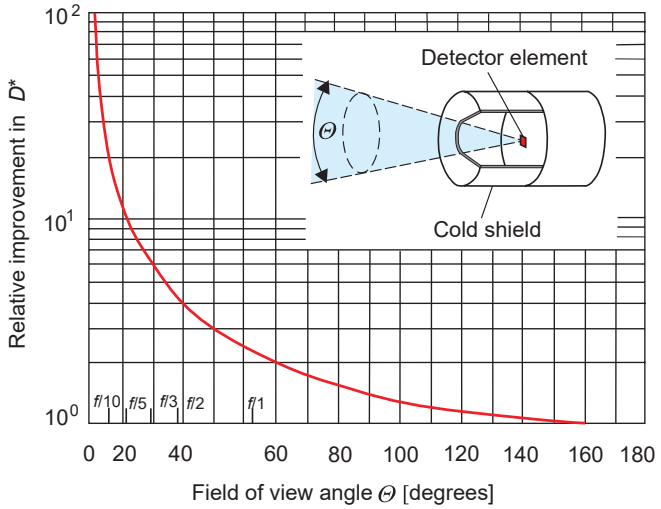


**Fig. 12.** Improvement in BLIP detector detectivity with a reduction in FOV cone angle

### 2.35. Field of view

The angular field of view is the maximum cone angle at which a detector can capture incoming radiation.

### 2.36. Linearity range

A linear photodetector generates photocurrent proportionally with the incident light power. Measurement of its linearity is accomplished by attenuation of the incident optical power.

The range of linear operation of the photodiode is defined, relating the two limits of the range to the required precision of the measurement. NEP and the maximum permissible deviation in the transition region from linear operation to saturation are given two limitations. It is also dependent on external circuit performances (load resistance).

### 2.37. Photodiode saturation and noise floor

Saturation occurs when the photocurrent at the photodiode output does not increase as the incident optical power increases. The saturation limit of the photodiode depends on the reverse bias voltage and load resistance (Fig. 13). The noise floor of a photodiode detection system depends not only on *NEP* of the photodiode but also significantly on load resistance. Some parameters affect the noise floor and saturation limit, e.g. detector temperature, resistivity, bias voltage, responsivity and bandwidth. Typically for systems with continuous-wave lasers, the system noise floor is limited to Johnson noise [20].

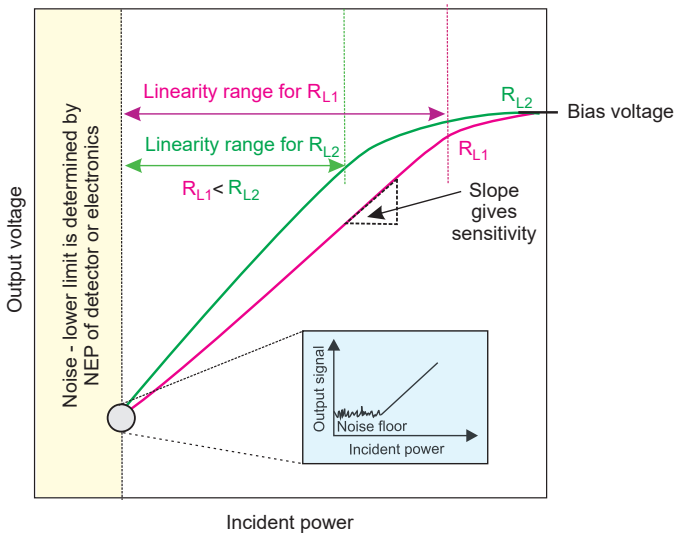


**Fig. 13.** Linearity response of a photodiode

### 2.38. Directional characteristics

The lens shape generally defines the directional characteristics. Figure 14a shows an example of narrow directional characteristics, and Fig. 14b illustrates an example of broad directional characteristics.

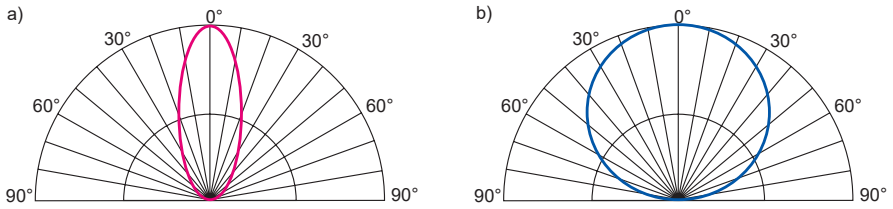


**Fig. 14.** Directional characteristics of a photodiode: a) narrow, b) wide characteristics

## 3. MEASUREMENTS OF DETECTOR PARAMETERS

To measure detector parameters, in addition to the electronic measuring devices, the following ones are necessary: a blackbody, modulated source of radiation with adjustable frequency, source of monochromatic radiation, and a reference detector. Electronic measuring devices include the following instruments: preamplifiers, lock-in amplifiers, and Fourier transform infrared (FTIR) spectrometers. Auxiliary measuring devices are, e.g. signal generators, calibrated attenuators and low-noise supply systems.

The detector signal depends on bias voltage $V_b$, the power of the incident radiation $\Phi_e$, the active area of the detector $A_d$, wavelength $\lambda$, signal modulation frequency $f$ and temperature $T$. In many cases, the expression for the detector signal can be separated as follows:

$$V_s(V_b,\Phi_e,A_d,\lambda,f,T) = u(V_b,\Phi_e,A_d,T)\,u(\lambda)u(f). \tag{32}$$

Assuming that the incident radiation power, the detector area and temperature are constant, then the above expression takes the form of:

$$V_s(V_b,\lambda,f) = u(V_b)\,u(\lambda)u(f). \tag{33}$$

Thus, three independent characteristics of $u(V_b)$, $u(\lambda)$ (called spectral) and $u(f)$ (called frequency) are obtained, which can be measured independently.

### 3.1. Current-voltage characteristics measurements

The current-voltage characteristics can be measured using either a specialized curve tracker or an ammeter and voltmeter.

Most test circuits allow either for source current and measure voltage (Fig. 15a) or for source voltage and measure current (Fig. 15b). A high impedance voltmeter must be used. Dark reverse current measurements must be carried out in complete darkness, especially for VIS detectors.

The circuit used in dark current measurement can also be applied to photocurrent measurements. In this situation, the photodiode is irradiated, and a current sampling resistor of lower value should be used because of the higher currents involved (Fig. 15c). The open-circuit voltage, $V_o$ and short-circuit current, $I_{sh}$, of photodiodes are measured, employing the circuits shown in Fig. 16. The open-circuit voltage $V_o$ of a photodiode can be measured with a high-sensitivity, high-resistance voltmeter.

The short-circuit current of the photodiode is measured by a current-to-voltage $(I-V)$ converter (Fig. 16b). To determine

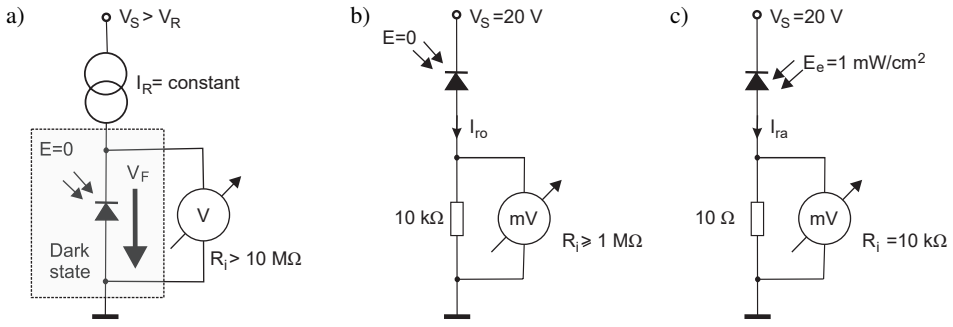


**Fig. 15.** Equivalent small-signal circuit of a photodiode (where $I_d$ – diode current, $I_{\mathrm{Rsh}}$ – shunt resistance current, $I_o$ – output current)

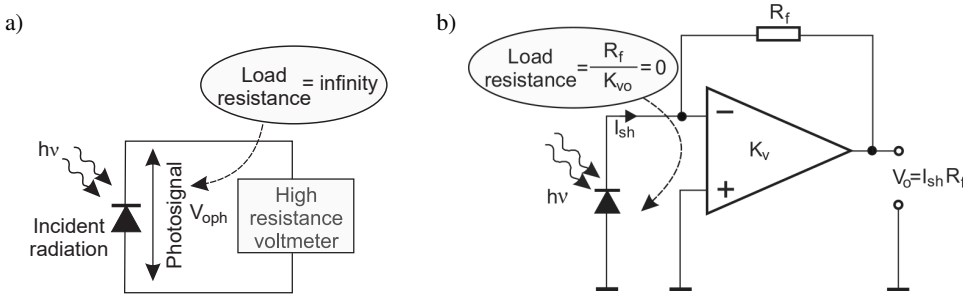


**Fig. 16.** Open circuit voltage (a), and short current (b) of photodiodes measurement characteristics (adopted after [22]).

the $I_{sh}$ current, it is necessary to measure voltage $V_o$ at the output $I$–$V$ converter and calculate the photodiode current by the following formula:

$$I_{sh} = \frac{V_o}{R_f}. \tag{34}$$

The amplifier and the feedback resistor appear as a photodiode load impedance of $R_f/K_{vo}$, where $K_{vo}$ is the amplifier's open-loop gain. Short-circuit impedance across the photodiode is very low because of the high value of $K_{vo}$ (of the order of $10^6$) as compared with the typical values of the photodiode's shunt resistance. For example, Fig. 17 shows the circuit diagram to evaluate photodiode characteristics using high resistance meter of the B2985A/87A type. The test system consists of the voltage source and an ammeter. The voltage source can sweep voltage while the ammeter synchronously measures the current. Therefore the photodiode current-voltage ($I$–$V$) characteristics can easily be obtained. In addition, the B2985A/87A can display the results as an X-Y graph. Detailed information about this meter is given in Technical Overview Keysight Technologies [23].

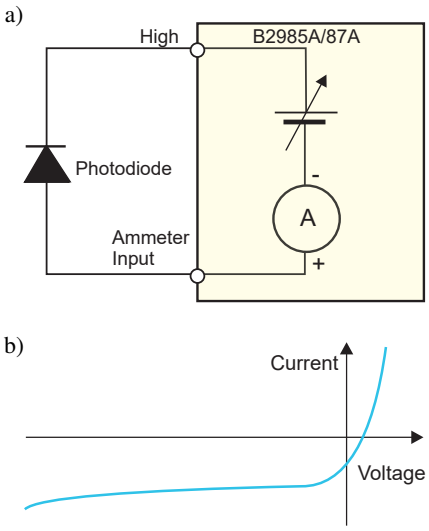


**Fig. 17.** Current diagram (a) used to evaluate photodiode $I$–$V$ characteristics (b)

### 3.2. Measurement of the impedance of detectors

Impedance characteristics can be measured with impedance analyzers (e.g. Agilent E4294A). Sometimes, there is a need to apply special measurement techniques and take necessary precautions against different measurement error sources because of the photodetector's capacitance and the measurement frequency. Detailed information is given in the literature [24].

As mentioned before, the inverse slope of the photodiode's $I$–$V$ curve at the 0 V point defines its shunt resistance (Fig. 18). However, slope determination is time-intensive, so it is measured at $V = -10$ mV in practice. Applying Ohm's law, shunt resistance $R_{sh}$ is calculated:

$$R_{sh} = \frac{\mathrm{d}V}{\mathrm{d}I}. \tag{35}$$

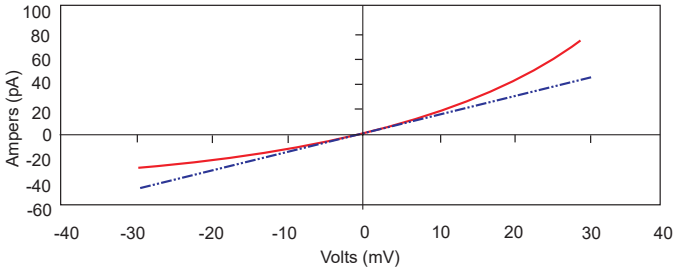


**Fig. 18.** Shape of the photodiode's $I$–$V$ curve with its linear fit (shunt resistance)

During the measurements, light input must be constant. The industry measurement method does not result in particularly accurate measurements. For better accuracy, the tangent to the measured $I$–$V$ curve should be determined. Detailed information is provided in paper [25].

Figure 19 shows logarithm $I$–$V$ characteristics of both ideal and real photodiodes and the method of determining both values of the aforementioned parasitic resistances. Three regions are visible. The ideal diode characteristics subjected to charge-carrier diffusion are observed in the middle region. In regions 1 and 3, the real characteristics show a deviation from the ideal one: in the range of small currents, due to shunt resistance, and for high currents, due to series resistance.

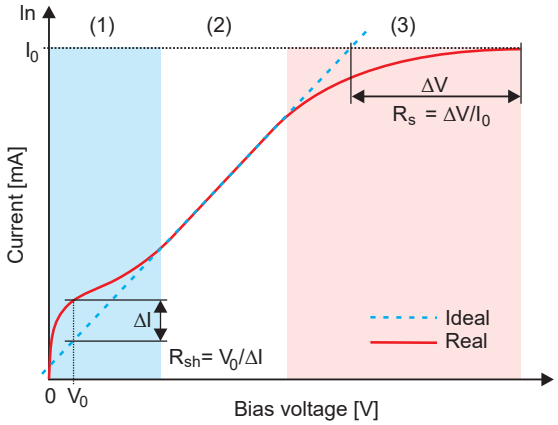


**Fig. 19.** Ideal and real current-voltage characteristics of forward-biased photodiode (adapted from [26])

### 3.3. Responsivity measurements

Spectral responsivity of detectors is defined and measured differently depending on the spectral range. For detectors operating in the visible and near-infrared range ($< 2.0$ μm), the spectral characteristic or $\lambda_p$, at which the detector has maximum sensitivity, is given. In the latter case, wavelengths for which sensitivity decreases to 10% of the maximum value should be reported. For these detectors, current responsivity $R_i$ in A/W is given. This is due to the relatively high impedance of the detectors and potential errors in measuring voltage responsivity (instruments with high ohms per volt $Q$ factors of 1 GΩ/V are required). Other reasons for measuring current responsivity are significant: linearity range response, wider bandwidth, and no dependence on detector capacitance.

The longer wavelength infrared detectors are usually characterized by low resistance. Therefore, to measure the voltage responsivity $R_v$ of these detectors, it is necessary to use an instrument that measures a voltage signal with an input resistance much greater than that of the detector. A simple relationship exists between these quantities:

$$R_v = R_d R_i \,, \tag{36}$$

where $R_d$ is the detector resistance. This condition is valid when the measured values refer to the same detector operating conditions (supply voltage and current).

Usually, spectral responsivity or responsivity to blackbody radiation of detectors are given. Let us take a closer look at how to measure both types of responsivity.

#### 3.3.1. Measurement of spectral responsivity with FTIR spectrometers

Responsivity measurements are essential for characterizing photodetectors. During this procedure, the tested detector works in the linear operation range [27]. The precise determination of its spectral characteristic makes it possible to estimate the power of the incident radiation based on the output signal. This characteristic is shaped both by the material parameters of the detector itself and the used optical system integrated with it (e.g. AR coatings, immersion lenses, optical windows, optical filters) as well as structure configuration (e.g. backside-illuminated).

In practice, applying reference radiometers or reference detectors generally provides lower measurement uncertainties as compared to reference radiation sources (blackbody or lamps). In this setup, photodetectors' calibration transfers the responsivity function from the reference device to the calibrated one. Usually, a silicon trap detector in the visible range and pyroelectrics in the infrared spectrum are used.

After calibration, the detector becomes a reference and allows for measurement of the energy parameters of the beam. They are usually defined as the quotient of the measured electrical signal (voltage or current) and the responsivity value. Such responsivity may refer to power, irradiance, or radiance. For an ideal radiometer, responsivity can be defined by the ratio of radiation responsivity to the detector's active area and its viewing angle. Detector calibration is related to the concepts of relative or absolute responsivity and uniformity, aperture effective area measurement, spectral linearity as well as temporal and temperature characteristics. Optical radiometry, photometry, colorimetry, temperature measurements of blackbody radiators, optical pyrometry and solar photovoltaic quantum efficiency measurements all allow for measuring responsivity. Two spectrometric systems, a monochromator or FTIR configurations, are often used to measure spectral responsivity. In addition, there are also some analytical setups for determining the discrete point of spectral characteristics of the tested detectors. Selective radiation sources (lasers) or thermal sources equipped with a dedicated set of optical filters are used in these setups. The last calibration method uses broadband radiation sources equipped with the estimated procedure of responsivity determination.

Depending on the configuration, laser sources, synchrotron radiation sources or thermal radiation sources (e.g. tungsten halogen lamps, Globars) provide different spectral ranges for absolute responsivity calibrations [28]. However, exact measurements require a large beam spot area of uniform optical radiation or a narrow uniform beam scanned across the component. Additionally, the beam used should have a narrow spectral bandwidth and be wavelength-tunable.

As the primary standard, some international standard organizations, such as the National Institute of Science and Technology, National Physical Laboratory, and Physikalisch-Technische Bundesanstalt, have used absolute cryogenic radiometers (ACR). Usually, in ACR, thermal detectors (thermopile and pyroelectric ones) with flat spectral responses are applied. They are a type of electrical substitution radiometers (ESR) with uncertainty below 0.01%. For that reason, a series of transfer detectors with stable radiation standards were also developed. However, their accuracy is not so high. The international practice uses the Si or InGaAs trap detector (uncertainty of about 1%), from visible to near-infrared bands. Calibration uncertainty of about 3% is ensured in the thermal infrared band by applying InSb and HgCdTe detectors.

Literature analysis has shown that there are many photodetector calibration systems. Based on their operation principle, a methods classification has been proposed:

- discrete calibration,
- spectrometric calibration,
- estimated calibration.

Detector responsivity at several wavelengths with a defined spectral linewidth is determined during discrete calibration. The measuring system defines the spectral parameters of the radiation. In this system, monochromatic sources (lasers) or radiation sources equipped with sets of optical filters can be used. Spectral responsivity is measured at discrete wavelengths during the first calibration step. And spectral characteristics are interpolated over the wavelength range using a physical or mathematical model.

In spectrometric calibration, the wide spectral radiation from a thermal or lamp source is spectrally shaped using the monochromator or interferometer in this setup. The filtered radiation is characterized by the referenced detector and then irradiated by the tested detector (device-under-test – DUT). Spectral responsivity is determined based on the known radiation spectrum and the DUT output signal.

Spectral response can also be estimated without the need for an expensive monochromator or a circular filter. Liberati described this method in [29]. It is based on analyses of detector signal changes resulting from temperature variation of a blackbody source. The responsivity determination requires solving a Fredholm integral equation of the first kind as a combination of the Planck radiation law and the detector's spectral response. This method can be used for non-defined infrared detectors (without data on their cut-off wavelength or spectral range of responsivity).

Figure 20 shows an example of a spectrometric calibration setup with a monochromator. The measuring system consists of a radiation source, optical system, modulator, monochroma-

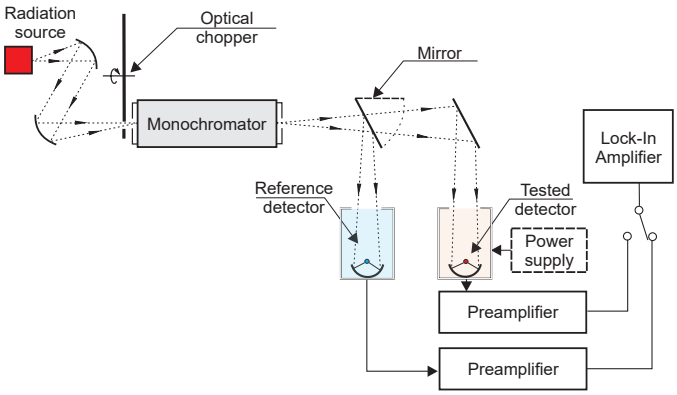


**Fig. 20.** Diagram of the system for measuring the spectral characteristics of the detectors

tor, detectors (reference and tested one) and signal amplification systems. Spectral responsivity is based on an output voltage of the preamplifier connected to the detector and radiation parameters (power, wavelength).

The monochromator light power is measured using a reference detector with known spectral sensitivity characteristics, e.g. a pyroelectric detector with a flat spectral responsivity characteristic.

The following procedure should be followed to determine current responsivity of the detector:

I) the radiation beam is switched to the reference detector and, then, to the tested detector using a suitable optical system,

II) if we have measured the voltage signals at the transimpedance preamplifiers output of the reference detector $V_r(\lambda)$ and the tested $V_s(\lambda)$, and we know the current responsivity of the reference detector $R_{ir}(\lambda)$, then we can calculate the current responsivity of the tested detector $R_i(\lambda)$:

$$R_i(\lambda) = R_{ir}(\lambda)\frac{V_s(\lambda)}{V_r(\lambda)} = R_{ir}(\lambda)\frac{I_s(\lambda)R_f}{I_r(\lambda)R_f} = R_{ir}(\lambda)\frac{I_s(\lambda)}{I_r(\lambda)}. \tag{37}$$

In practice, the relative spectral characteristics of the detector are often given. Such characteristics are obtained by dividing the responsivity of the detector $R_i(\lambda)$ by its maximum value $R_{i\max}(\lambda_o)$:

$$R_{i\%}(\lambda) = \frac{R_i(\lambda)}{R_{i\max}(\lambda_o)}100\%. \tag{38}$$

Nowadays, spectral responsivity of IR detectors is usually measured using an FTIR spectrometer. Commercial FTIR spectrometers are developed for transmission measurement and not for photocurrent spectroscopy of photodetectors (PDs). To acquire the response spectrum of PD using an FTIR spectrometer, the PD should be inserted into the light path of the sample compartment with an optional external detector port to receive interferential light. The main advantage of such measurement is high spectral resolution, relatively high radiation power and short measurement time. The possibility of signal averaging also results in an improvement in the signal-to-noise ratio.

The typical FTIR spectrometer consists of a light source, a diaphragm limiting the aperture of the source, an interferometer, sample compartment, internal detector, amplifier, and a computer (Fig. 21). The light source generates radiation that irradiates the sample (DUT), passes through the interferometer, and reaches the detector. Then the signal is amplified and converted to a digital form (interferogram). In another way, the interferogram is transferred to the spectrum using a fast Fourier transform (FFT) algorithm. It converts the intensity-versus-time spectrum into an intensity-versus-frequency one. Thus, the FTIR spectrometer collects the interferogram, performs the FT function, and displays the spectrum. The core of the FTIR spectrometer is the Michelson interferometer. It consists of a beam splitter, a fixed mirror and a moveable mirror that translates back and forth in a precise manner. One beam is transmitted through the beam splitter to the fixed mirror, and the second is reflected off the beam splitter to the moving mirror. The fixed and moving mirrors reflect the radiation to the beam splitter. Accordingly, these reflected radiations are recombined at the beam splitter, resulting in one beam leaving the interferometer and illuminating the detector.

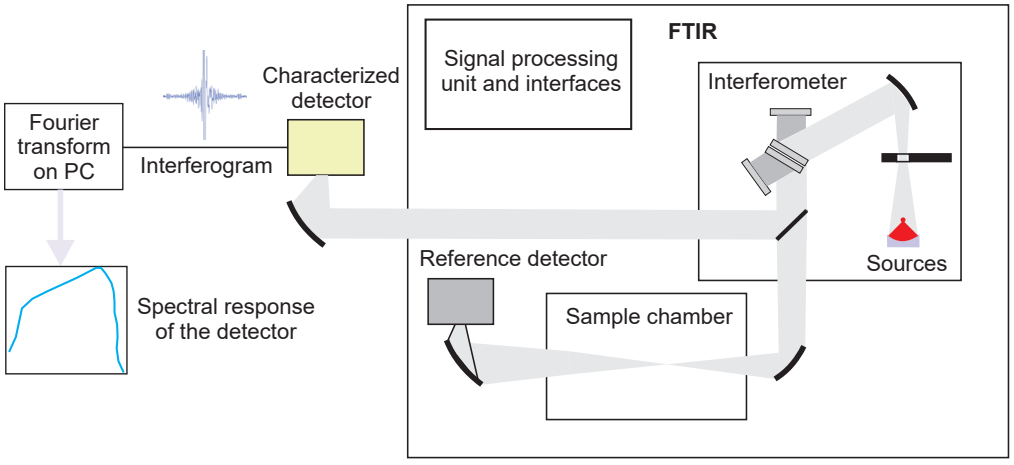


**Fig. 21.** The principle of determining the spectral response of a detector using FTIR measurement

Consequently, the detector simultaneously registers variation in energy-versus-time for all wavelengths. The output intensity changes interferences by varying the optical path difference $\delta$ with a movable mirror. The Fourier transform of the registered interferogram $I(\delta)$ gives the measured spectrum $S(\sigma)$:

$$S(\sigma) = \mathrm{FFT}\{I(\delta)\}, \tag{39}$$

where $\sigma$ is the wavenumber usually expressed in $\mathrm{cm}^{-1}$. The measured signal $M(\sigma)$ is the product of the researched spectrum by the temporal transfer function of the detector $H(R, f_e, \sigma)$:

$$M(\sigma) = H(R, f_e, \sigma) \times S(\sigma), \tag{40}$$

where $f_e$ is the sampling frequency of the interferometer and $R$ stands for the "retardation rate" of the spectrometer. Its value relies on the wavelength of the laser used to measure the interferometer displacement $R = \lambda_{\mathrm{las}}/2$.

A simple linear transfer function determines the ratio between measurement and baseline during comparative research with the same detector (e.g. transmission). However, during spectral characterization of an outside IR detector, the detector transfer functions differ between the baseline and the detector measurement itself. For a not-so-fast detector (e.g. pyroelectric one) used as a reference detector, this temporal-spectral range is critical.

This proves the need for correction of this detector transfer function in the case of spectral response measurements. Additionally, significant distortions of the spectral characteristics can be caused by the detector response non-linearity. There are different approaches (hardware and software) to solve the non-linearity problem [30, 31]. Unlike the monochromator systems, changing the reference detectors during measurement in a given spectral range is impossible.

Summary of the properties of some photodetector calibration systems is provided in Table 2.

**Table 2**
Main virtues of some spectroradiometric services

| No. | Reference detector applied | Mode | Spectrum | Source | Uncertainty | Literature |
|---|---|---|---|---|---|---|
| 1 | Pyroelectric radiometer | Discrete | 800–2000 nm | tunable supercontinuum laser 2.5 mW | 4% to 2.2–2.6% | [32] |
| 2 | – | Discrete | 1.5 µm,<br>2.7 µm,<br>3.9 µm,<br>10.6 µm,<br>14 µm | blackbody 1–20 µW with filters | 7.5%,<br>8.8%,<br>5%,<br>5.1%,<br>19% | [33] |
| 3 | Radiometer | Discrete | 3.96 µm,<br>9.45 µm,<br>10.6 µm | QCL, $CO_2$ laser / 1 µW, and more 1 mW. | 6.1%,<br>6.0%,<br>2.5% (1.4%) | [34] |
| 4 | Silicon photodiode | Discrete | 543.5 nm | low-cost green He–Ne lasers 0.13 mW | 0.009% | [35] |
| 5 | Radiometer | Discrete | 450–800 nm | dye laser with integrated sphere | 0.04% | [36] |
| 6 | Radiometer | Discrete | 406.74 nm<br>441.57 nm<br>487.99 nm<br>532.08 nm<br>632.82 nm<br>769.64 nm | Kr+<br>He–Cd<br>Ar+<br>doubled Nd:YAG<br>He–Ne<br>Ti-sapphire | 0.027%<br>0.028%<br>0.030%<br>0.042%<br>0.034%<br>0.029% | [37] |
| 7 | Radiometer | Spect.–Mono | 3–25 eV<br>40–1.5 keV | electron storage ring BESSY 1–10 µW | 1% | [38] |
| 8 | Estimation | Estimated | | blackbody | – | [29] |
| 9 | Reference detector | Spect.–Mono | 1.5–15 µm | silicon-carbide bar thermal source tungsten–halogen lamp | 5% | [39] |
| 10 | DTGS | Spect.–FTIR | Up to 20 µm | Globar halogen lamp | – | [40] |
| 11 | Radiometer | Discrete | (7.35–10.6) µm | tunable QCL | 0.097%–0.16% | [41] |
| 12 | DTGS | Spect.–FTIR | 1.5–18 µm | Globar | 1–2% | [42] |

### 3.3.2. Measurement of detector responsivity to blackbody radiation

An example of the measuring system designed to measure the responsivity of infrared detectors to blackbody radiation is shown in Fig. 22. In this case, the blackbody replaces the monochromator with a suitable radiation source. This system uses a blackbody equipped with conical cavity. The special shape of the blackbody cavity, the selected ratio of its dimensions and the diameter of the iris cover ensure high emissivity of the effective radiation source ($\varepsilon = 0.998$). The radiating cavity is heated to the required operating temperature by means of resistance heaters.

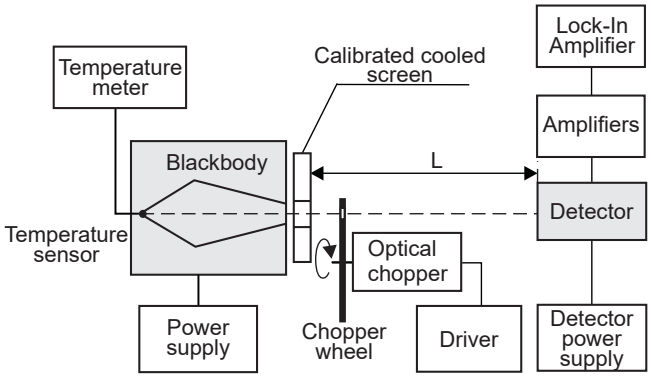


**Fig. 22.** System for measuring responsivity of detectors to blackbody radiation

Many detectors require an external power supply. For this reason, the detector power supply range is determined. Efforts should be made to ensure that the value of the detector supply current is adequately selected. Excessive bias current can cause thermal instability of the detector and increased noise. On the other hand, a low bias current value will not provide a sufficient signal-to-noise ratio. The manufacturer usually specifies the highest allowable power supply voltage or maximum detector current. If measurements are carried out with a supply voltage greater than that specified by the manufacturer, they shall be carried out following the safety rules. The detector bias voltage should then be changed by a small value while observing the noise level. If the supply voltage or current is higher than the limit value, a slight increase in the supply current and noise level will be observed. The excess bias of the detector may lead to system instability or detector destruction.

The value of the radiation flux incident perpendicular to the detector area should ensure linear detector operation.

Detector responsivity at constant frequency-modulated radiation is most often measured to minimize the influence of its bandwidth. A mechanical modulator (chopper) of the radiation beam and a lock-in amplifier or a spectrum analyzer are used.

The analyzer center frequency is equal to the frequency of the chopper. For acoustic and sub-acoustic frequencies, mainly mechanical modulators are used. Modulation frequencies higher than 50 kHz are challenging due to the need to use discs with large diameters, small slot sizes and high spin speeds.

Rectangular modulation is most often used, so it is assumed that the power of the fundamental component of the modulation waveform Fourier expansion is given ( modulation frequency is understood as the fundamental frequency). For spectral measurements, the modulator should be placed at the input slot of the monochromator. And it should be able to adjust the frequency.

The density of the radiation flux incident on the detector active area should be uniform. If the radiation reaches only a part of this area, the signal may depend on the position of the illuminated field.

The Stefan–Boltzmann equation determines the power radiated through the source outlet:

$$P_R = \sigma \left[ \left( T_R^4 - T_B^4 \right) A \right], \tag{41}$$

where $T_R$ is the source operating temperature, $T_B$ is ambient temperature, and $A$ is the hole surface.

The power of the radiation irradiating detector is determined by irradiance $E_e$ and detector area $A_d$:

$$P_o = A_d E_e, \tag{42}$$

and the power delivered to receiver $P_s$, set on the optical axis at the measuring distance $L$ from the calibrated outlet screen, is determined by the following equation:

$$P_s = P_R \frac{A_d}{\pi L^2}. \tag{43}$$

With the measured RMS value of the voltage at the detector output $V_s(V_b, f)$, it is possible to calculate the detector voltage sensitivity to blackbody radiation:

$$R_B(V_b, f) = \frac{V_s(V_b, f)}{P_s}. \tag{44}$$

The $R_B(V_b, f)$ measurements should be made for the full range of detector bias and operating frequency.

### 3.4. Noise measurements

Noise measurements in optical detectors effectively determine their detectivity, material quality and reliability. The direct measurements of noise characteristics are the only reliable way to estimate device detectivity, which is inversely proportional to the detector's noise. Defects in microstructure can also be examined using proper interpretations of noise measurements results. Precisely selected bias parameters are often required to obtain optimum detector performances. This condition is a specific compromise also taking account of noise intensity. The proper example of such a situation is biasing the photoconductors, which need to be supplied to produce output signals. Lower capacitance and shorter rise time can be obtained by applying bias for photovoltaic devices. For that reason, the noise measurements of the optical detectors are important, and they have been developed for years [43–46].

Due to their random nature, noises are subject to the statistical description used to analyze stochastic processes. Therefore, the measurement of noise signals requires methods and apparatus other than those used in the measurement technique of

deterministic signals. In particular, it is necessary to eliminate the influence of external disturbances. Interferences transmitted through the electrical network are particularly difficult to eliminate. The detector noise depends mainly on its temperature and applied bias. These conditions also cause change in detector parameters such as impedance (shunt resistance, junction capacitance), rendering detector noise measurements and calculations more complicated.

Noise measurements can be divided into noise current measurements and noise voltage measurements. The noise current is measured with current-mode readout and noise voltage – with a voltage-mode amplifier. The results obtained for both types of noise from resistance type fluctuations are generally equivalent and can be interchangeably converted using detector impedance. Selection of the appropriate method depends mainly on detector impedance and noise level of the measurement system. In the case of low impedance detectors (below few kΩ), voltage noise measurements are recommended because of lower system noise. For high impedance detectors (few kΩ and more), current noise measurements are a better choice. The scheme of a typical noise measurement system is presented in Fig. 23.

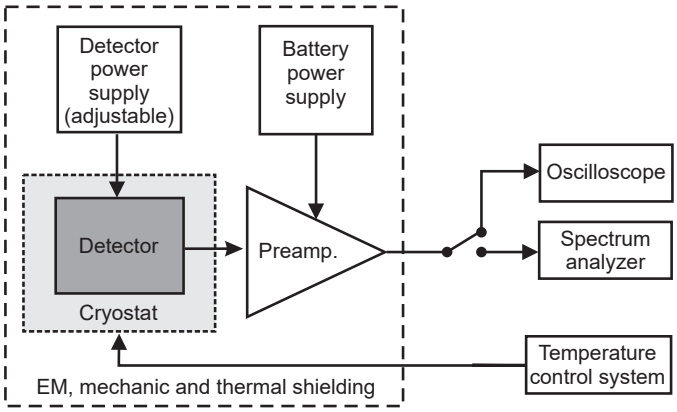


**Fig. 23.** Block diagram of a system for measuring detector noise

All system elements have a significant impact on its capabilities and measurement results. The detector power supply circuit should be characterized by low output noise. An effective way to reduce power network interferences (50 Hz and its derivatives) is to bias the detector and preamplifier from the battery sources. The detector, preamplifier and power supply should be placed in a common, shielded housing, effectively attenuating low external interference from the main network and high frequencies from devices such as voltage converters. Moreover, the shielding apart from electromagnetic interferences (EMI) should also ensure mechanical isolation from vibrations. Stable temperature of the sample is also required to obtain reliable results.

The current source should be used during noise voltage measurement and the voltage source should be used in the case of noise current measurements. Excessive noise from the detector power supply can be detected if a low noise (metal) resistor with resistance equal to detector resistance is connected to the measurement system instead of the detector. Resistor noise shall be independent of the flowing current (low flicker noise).

A broadband oscilloscope or spectrum analyzer is usually used to observe them. Some publications and datasheets present low noise voltage sources [47–52]. Such apparatus noise performance depends on the output voltage, load impedance and frequency. Their noise can be as low as 1 nV/$\sqrt{\text{Hz}}$ in the case of custom-designed circuits and about a few or few dozen nV/$\sqrt{\text{Hz}}$ in commercial devices, considering the frequencies of about 1 kHz. In the case of current sources, the noise also depends on the output current, load impedance and frequency. Consequently, an adequately selected device can obtain output current noise as low as a few pA/$\sqrt{\text{Hz}}$ [53–59].

The selected amplifier and its performances are crucial elements that usually set system capabilities, such as noise, bandwidth and input signal range. Generally, the two options are either a transimpedance amplifier (TIA, current to voltage converter) or a voltage amplifier. In both types, the type of input stage can be selected: with bipolar transistors (BJT), junction field-effect transistors (JFETs) or metal-oxide-semiconductor field-effect transistors (MOSFETs). Each performs differently, so appropriate selection depends on detector properties. But it must be highlighted that if high detector noise is expected as compared to the noise added by the system, it is not necessary to use an exorbitant measurement system. In the case of high impedance detectors under high bias conditions and intense noise generated by the detector, only an adequate spectrum analyzer (with low noise and sensitive input with a built-in amplifier) should be applied. Then, the amplifier can be omitted in the measurement setup. The performances of selected low-noise amplifiers are presented in Table 3. A few commercial devices and custom-designed devices that can be used for detectors' noise measurements were included in this summary.

Moreover, Table 3 shows that the lowest level of $I_n$ is associated with the MOSFET input stages, but the highest level of $V_n$ characterizes them. The BJT input stages generally allow to obtain a low level of $V_n$ but at the cost of a high level of current noise. Some specific compromise is obtained with JFET input ones, and for this reason, they are often used in amplifiers' input stages. The custom devices using low-noise JFETs lead to getting both: very low level of voltage and current noise. The temperature impact on noise measurements can be investigated using a few ways to control detector temperature. The detector sample can be placed on a thermoelectric cooler (TEC) or in a variable or constant temperature cryostat filled with liquid helium or nitrogen. It must be highlighted that the temperature should be time stable, and the additional control system cannot produce other interferences visible in the spectrum. Such a problem can be observed when some current pulse method of TEC control is used.

Noise voltage measurements can be made by observing the voltage preamplifier output signal with an FFT spectrum analyzer, oscilloscope, selective nano-voltmeter, lock-in amplifier, or selective (in the radio frequency range) micro-voltage meter. Attention should be paid to how the indicators of these instruments are calibrated. The signal observed by spectrum ana-

**Table 3**
Performances of selected low noise amplifiers

| Name | Type of amp. | Input type | $V_n$ [nV/$\sqrt{}$Hz] | $I_n$ [fA/$\sqrt{}$Hz] | Bandwidth [Hz] | Ref. |
|---|---|---|---|---|---|---|
| SR560 | Voltage | JFET | 5.5 at 10 Hz<br>4 at 1 kHz | not specified | 0.03 to $10^6$ | [60] |
| SR570 | TIA | JFET | not specified | 5 at 1 Hz (10 nA/V)<br>60000 at 1 kHz<br>(10 mA/V) | DC to $10^6$ | [61] |
| Sig. Rec. 5113' | Voltage | JFET | 4 at 1 kHz | not specified | DC to $10^6$ | [62] |
| Sig. Rec. 5182 | TIA | JFET | $\approx$ 3 at 1 kHz [72] | 10000 at 1 kHz<br>(10 µA/V), 15 at 1 kHz<br>(10 nA/V) | DC to $\approx 10^6$ | [63] |
| SIM911 | Voltage | BJT | 2 at 10 Hz<br>1.8 at 1 kHz | not specified | DC to $10^6$ | [64] |
| DLPCA-200 | TIA | JFET | 4 at 1 kHz | 4.3 at $10^9$ V/A<br>43 at $10^7$ V/A | DC to 0.5×$10^6$ | [65] |
| Custom design | Voltage | JFET | 0.6 at 10 Hz<br>0.5 at 1 kHz | not specified | 0.07 to 0.1×$10^6$ | [66] |
| Custom design | Voltage | JFET | 0.6 at 10 Hz<br>0.5 at 1 kHz | not specified | 0.2 to few $10^3$<br>(flat region) | [67] |
| Custom design | Voltage | JFET | 1 at 10 Hz<br>0.6 at 100 Hz | not specified | 0.02 to 0.6×$10^6$ | [68] |

lyzer input should be recalculated, taking into account its input impedance typically of 50 Ω or 1 MΩ. The RMS value can be specified in a given band using an oscilloscope. The frequency limiting to the interesting range can be made by connecting the signal filter between the preamplifier output and oscilloscope input or using built-in oscilloscope filters, if available. In the case of custom FFT analyzers (e.g. based on PC data acquisition cards), proper low-pass filtration of the signal to avoid antialiasing should also be ensured.

The FFT spectral resolution works out a compromise between the number of averages and measurement time. High FFT resolution results in a long time of sampling and averaging to obtain a smooth spectrum with narrow peaks due to the interferences depending on the type of EMI. However, it allows to easily interpret them as not related to the examined noise signal. The algorithm for pre-processing the measurement data (e.g. windowing) is critical before the FFT processing, and significantly impacts the final result.

In oscilloscope measurements, the main limitation is that only white noise can be efficiently specified using peak-to-peak (p–p) and RMS dependencies.

The lock-in amplifier can also measure noise in the time domain at the desired frequency in the selected filter bandwidth.

Figure 24 presents a typical detector-preamplifier circuit. It must be noted that the preamplifier should have high impedance and AC-coupled input in order not to saturate the output with the high DC component during biasing of the detector.

After turning on the low noise voltage source, the RMS noise voltage value at the preamplifier output $V_{\mathrm{no}}(V_b, f)$ should be

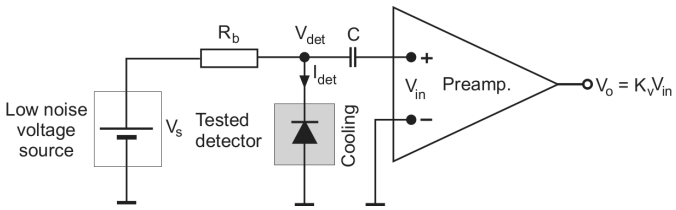


**Fig. 24.** Detector noise measurement circuit with voltage amplifier

measured as a function of frequency. It should be highlighted that the noise signal at the preamplifier output is composed of detector noise, amplifier noise (which also depends on detector impedance) and detector power supply noise. To precisely determine the self-detector noise, other components should be considered. In some cases, additional noise sources from the system can be assumed as negligible. Such a situation can be obtained when a medium impedance source is present at the low noise JFET amplifier input. It operates in a region where the noise figure has the lowest values. If it is not possible to ignore them, appropriate calculations which subtract additional noise sources from the system should be provided. In such a case, the detector should then be replaced by an equivalent metal resistor with resistance equal to the detector's dark resistance. Again, we measure the output noise voltage as a function of frequency. The value of this voltage is marked as $V_{na}(f)$.

After tuning the spectrum analyzer to the frequency of the calibration signal, the output voltage value $V_o$ should be measured. The measurements are made in the same frequency range

as before. The gain of the measuring system $K_v(f)$ should be measured and then used to include the system's frequency variable system gain/response characteristics.

The RMS value of the noise voltage of detector $V_{ni}$, related to the input of the photodetector-preamplifier system, is determined by the following equation:

$$V_{ni}(V_b, f, \Delta f) = \left[\frac{V_{no}^2(V_b, f, \Delta f) - V_{na}^2(V_b, f, \Delta f)}{K_v^2(f)} + V_J^2(\Delta f)\right]^{1/2}, \tag{45}$$

where $V_{no}$ is the RMS value of the noise voltage at the system output, and $V_J$ is the RMS value of the Johnson noise voltage generated by the detector in the noise bandwidth $\Delta f$. A more straightforward way is to provide noise measurements in the known flat frequency response region and skip the frequency response measurement. In this case, $K_v(f)$ can be extracted from hardware datasheets and assumed as a constant.

To calculate spectral density of the detector noise voltage, the obtained value of $V_{ni}$ should be divided by the root of the bandwidth $\Delta f$:

$$V_{ni}(V_b, f) = \frac{V_{ni}(V_b, f, \Delta f)}{\Delta f^{1/2}}. \tag{46}$$

The above equations are valid for a uniform noise voltage spectral density distribution.

Since the noise voltage depends on the detector power supply voltage, measurements should be taken for different values. Knowing the relationship between the signal-to-noise ratio and the detector supply voltage makes it possible to determine the optimal value of this voltage (e.g. for photoresistors).

With the primary noise sources occurring in the system in mind, a simplified noise scheme can be presented in Fig. 25. The noise source of the detector biasing circuit was omitted.

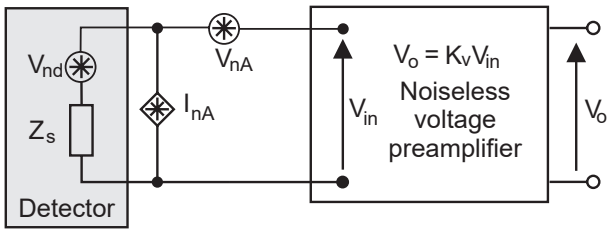


**Fig. 25.** Noise sources in detector noise measurement circuit with voltage preamplifier. $V_{nA}$ – voltage noise source of the amplifier, $I_{nA}$ – current noise source of the amplifier

The source of noise current of the amplifier ($I_{nA}$) is present at the amplifier output signal as a voltage of $K_v I_{nA} Z_s$. It can be easily noticed that this noise source can become dominant and significantly reduce system sensitivity for very high impedance sources. For low impedance sources, the limitation can come from amplifier voltage noise source $V_{nA}$, higher than measured detector noise, especially with low impedances and low biases when its noise ($I_{\mathrm{nd}}$) is weak. The measured power spectral density $S_v$ of the voltage referred to the preamplifier input is given by the following equation:

$$S_v = \frac{S_{vo}}{K_V^2} = S_{vnA} + S_{inA}|Z_s|^2 + S_{vnd}, \tag{47}$$

where $S_{vnA}$, $S_{inA}$ and $S_{vnd}$ are the power spectral density (PSD) of voltage noise $V_{nA}$, current noise $I_{nA}$ of the preamplifier and detector noise $V_{nd}$. $S_{vo}$ is the measured PSD at the preamplifier output. The noise voltage measurement can be effective in low impedance detectors when the noise current measurements systems are characterized by higher noise.

Yet another method is noise measurement using a transimpedance preamplifier. In this case, the low noise current to voltage $(I-V)$ converter is used to gain current fluctuations of the detector current. To determine the detector noise, the noise of the measuring system (floor noise) should be subtracted from the final results. The floor noise is composed of, e.g. amplifier noise current, amplifier noise voltage, feedback resistor current noise and biasing source.

Considering the measurement of voltage fluctuations (Fig. 24), a more complex method that reduces the system noise should be mentioned. The two-channel voltage correlation method eliminates the influence of the preamplifiers' noise voltage ($V_{nA}$). It can be convenient and helpful during very low impedance detectors tests, especially with low biases. In this case, the voltage noise from the preamplifier can be dominant and can significantly limit the measurement range. The typical block schematic diagram of a two-channel voltage cross-correlation system is presented in Fig. 26. The output signals $(V_1(t), V_2(t))$ from the two identical preamplifiers ($A_1$ and $A_2$) are antialiasing filtered ($\mathrm{AAF}_1$, $\mathrm{AAF}_2$) and simultaneously sampled by a two-channel data acquisition system with PCI-4462 card. Then the signals are processed using a cross-correlation procedure based on discrete Fourier transform (DFT) to obtain cross-spectrum estimation ($S_{12}$).

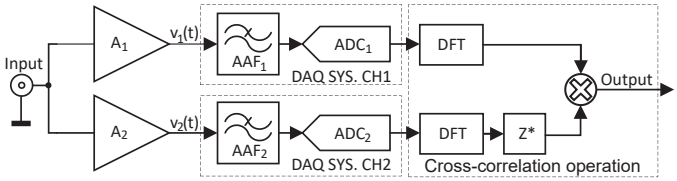


**Fig. 26.** Block schematic diagram of two-channel voltage cross-correlation measurement system [70].
$Z^*$ – complex conjugate

The implementation of this method used to measure noise in low impedance detectors is described in papers [69, 70]. The schematic diagram of the detector connected to the two-channel voltage cross-correlation system is shown in Fig. 27. The $R_1C_1$ filter was used in order to avoid saturating amplifier outputs. The ultra-low noise amplifiers combined with this method used in [69] lead to relatively quickly obtaining ultra-low noise levels of the system noise. This feature enables an investigation of detector noise with low biases in the wide frequency range, and the result can be obtained in a short time.

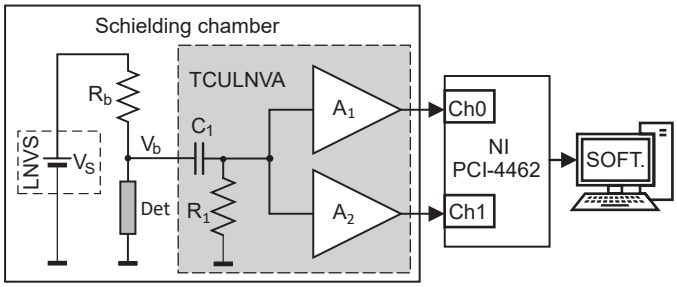


**Fig. 27.** Detector connection to two-channel voltage cross-correlation system [69]

This approach requires the current noise source of the amplifiers to become negligible, along with high impedance inputs (JFET, MOSFET based) and constant gains ($K_1 = K_2 = K$). Under these conditions, output voltages from the amplifiers can be given by:

$$V_{n1}(t) = KV_{nd}(t) + KV_{nA1}(t),$$
$$V_{n2}(t) = KV_{nd}(t) + KV_{nA2}(t). \tag{48}$$

Because the preamplifier voltage noise sources are uncorrelated, after calculating the cross-spectrum ($S_{12}$) from the two output signals ($V_{n1}, V_{n2}$), the examined detector noise can be determined using:

$$S_{nd} = \frac{S_{12}}{K^2}. \tag{49}$$

If the required averaging time is ensured, equivalent noise voltage sources are reduced to a level that can be assumed as negligible. This method enables to prepare reliable noise characteristics of a detector with resistances as low as a few Ohms. Moreover, at this point, it can be mentioned that noise measurements of low impedance detectors are difficult when using transimpedance systems because of high input DC. The noise of the transimpedance amplifier usually decreases when the transimpedance gain is increasing. However, it limits the maximum input current because of overloading amplifier output. On the other hand, reduction of transimpedance results in higher noise. These reasons cause the cross-correlation method to be more efficient in this specific case.

Figure 28 shows a schematic diagram of the measurement system, which allows for measuring not only noise characteristics of the detectors but also spectral characteristics and current-voltage characteristics of photodiodes. The idea of measuring the spectral and noise detector characteristics is analogous to the methods discussed above. Thanks to the use of helium cryostat, nitrogen cryostat, Peltier module and high-temperature module, it is possible to measure the parameters and characteristics of the detectors in the temperature range of 10–450 K.

Keithley's 236-type precision source-measure unit measured photodiodes' current and voltage characteristics. It enables the imposition of voltage extortion and current measurement, or current extortion and voltage measurement. The photodiode is reverse biased by an adjustable DC voltage source connected to a non-inverting element of the current-to-voltage converter.

Analyses of noise measurement in detectors allow for determining some system's performances and test conditions (Table 4). The types of examined detectors, their resistance and their bias were all considered [69].

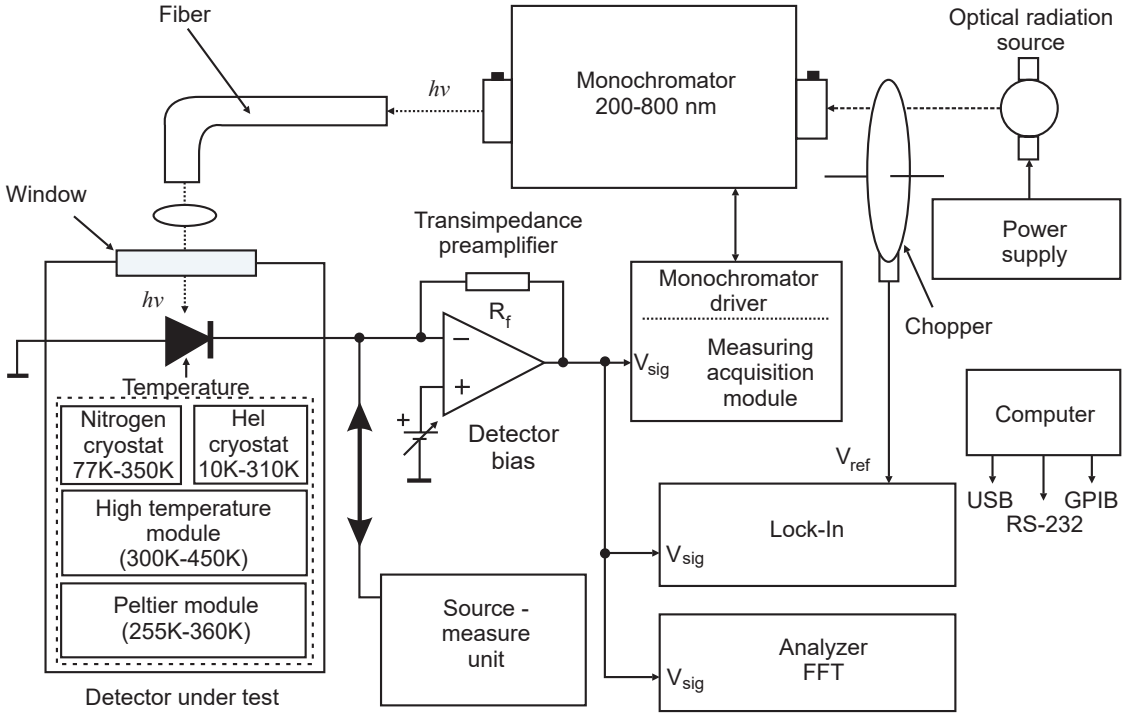


**Fig. 28.** The scheme of the measurement system that enables the measurement of spectral characteristics of detectors, current–voltage characteristics of photodiodes, and noise characteristics (after [71])

**Table 4**
Performances of IR photodetectors noise measurements

| Type of the meas. detectors | Detector resistances | Type of measured fluctuations /methods | Model of the front-end preamp. | Meas. system noise (preamplifiers) | Meas. band-width | Range of bias (rev.) | Ref. |
|---|---|---|---|---|---|---|---|
| InAsSb | $\approx 4\ \Omega$ and 6 Ω [300 K] | voltage/two channels with cross correlation | custom design | $V_{nA}^2 = 3 \times 10^{-19}$ V$^2$/Hz at 1 kHz<br>$V_{nA}^2 = 1.5 \times 10^{-17}$ V$^2$/Hz at 1 Hz | 0.1 to 100 kHz | 1.7 mV to 216 mV | [69] |
| InAs/ InAs Sb SL | $\approx 5\ \Omega$ and 11 Ω [300 K] | voltage/two channels with cross correlation | SR 5186 | $V_{nA}^2 = 1.6 \times 10^{-17}$ V$^2$/Hz at 1 kHz | 1 Hz to 1 kHz | ≈ 90 to 800 mV | [70] |
| HgCdTe, InAs/GaSb T2SL | ≈ 60 Ω to above 1 MΩ (dynamic resistance) | current/single channel | TIA EG&G 5182 | $V_{nA}^2 = 1 \times 10^{-17}$ A$^2$/Hz at 100 Hz<br>$I_{nA}^2 = 2 \times 10^{-27}$ A$^2$/Hz [$10^8$ V/A] at 1 kHz | 1 Hz to 10 kHz | 1.5 mV to 1 V | [72] |
| p-InAsSbP/ n-InAs | $R_0 \approx 10^3\ \Omega$ [300 K] | voltage/single channel | EG&G 5113 | $V_{nA}^2 = 1.6{\times}10^{-17}$ V$^2$/Hz at 1 kHz | 0.5 Hz to 10 kHz | ≈ 40 pA to 1 μA | [73] |
| InAs/GaSb SL | – | current/single channel | TIA Keithley 428 | $I_{nA} = 90$ nA$_{rms}$ at $10^3$ V/A<br>$I_{nA} = 1.2$ fA$_{rms}$ at $10^{11}$ V/A | 0.3 to about 200 Hz | 100 to 800 mV | [74] |
| InAs/GaSb SL | – | current/single channel | TIA DDPCA-300 | $I_{nA}^2 = 2 \times 10^{-21}$ A$^2$/Hz [$10^4$ V/A] at 10 Hz<br>$I_{nA}^2 = 4 \times 10^{-30}$ A$^2$/Hz [$10^{12}$ V/A] at 10 Hz | 1 to 20 Hz | 0.2 to 0.9 V | [75] |
| InAs/GaSb SL | – | current/single channel | TIA DLPCA-200 | $V_{nA}^2 = 1.6 \times 10^{-17}$ V$^2$/Hz at 1 kHz<br>$I_{nA}^2 = 4 \times 10^{-22}$ A$^2$/Hz [$10^3$ V/A] at 10 kHz<br>$I_{nA}^2 = 1.85 \times 10^{-29}$ A$^2$/Hz [$10^{11}$ V/A] at 100 Hz | 1 Hz to 8 kHz | 0.05 to 0.8 V | [76] |
| Film–Si Schottky barrier CNT | – | voltage/single channel | TIA SR560 | $V_{nA}^2 = 1.6 \times 10^{-17}$ V$^2$/Hz at 1 kHz | 1 to 100 Hz | 0.46 to 2.85 V | [77] |
| PbS Photo-conductor | ≈ 60 kΩ to 5 MΩ | current/single channel | TIA DLPCA –200 | $V_{nA}^2 = 1.6 \times 10^{-17}$ V$^2$/Hz at 1 kHz<br>$I_{nA}^2 = 4 \times 10^{-22}$ A$^2$/Hz [$10^3$ V/A] at 10 kHz<br>$I_{nA}^2 = 1.85 \times 10^{-29}$ A$^2$/Hz [$10^{11}$ V/A] at 100 Hz | 500 Hz to 5 kHz | 2 to 6 V | [78] |
| PNP PIN Photo-transistor | – | current/single channel | TIA LT1124 | $V_{nA}^2 = 7.29 \times 10^{-18}$ V$^2$/Hz<br>$I_{nA}^2 = 9.07 \times 10^{-26}$ A$^2$/Hz | 10 Hz to 700 kHz | 100 nA to 2 μA | [79] |

### 3.5. Measurement of frequency characteristics

The frequency response is usually measured by analyzing the time response of photodetectors detecting the optical pulse or by the measurement of directly or externally modulated laser radiation [80]. Some other frequency response methods have also been studied, e.g. pulse spectrum analysis, two-tone method, heterodyne detection, shot-noise spectrum, or white optical noise [81].

The rise and fall times of the detector response can be determined using rectangular optical pulses in the system shown in Fig. 29.

This system consists of a pulse generator and laser diode LD or LED, tested photodiode (PD) as well as an oscilloscope. The LED or laser diode is pulse-powered from a generator and illuminates the photodiode. The output signal from the photodiode is measured at load resistance of 50 Ω, with a broadband

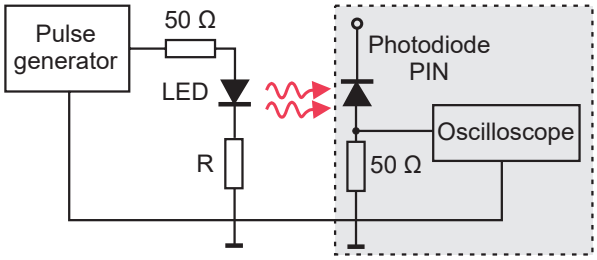


**Fig. 29.** System for determining the rise and fall time of photodiode output signal, which comes in response to rectangular pulse excitation

oscilloscope. Based on the measured pulse fall time $t_f$, the photodiode time constant $\tau_d$ can be determined from the following equation:

$$\tau_d = \left( \left( \frac{\tau_f}{2.2} \right)^2 - \tau_{amp}^2 - \tau_{osc}^2 \right)^{1/2}, \tag{50}$$

where: $\tau_{amp}$ – preamplifier time constant, $\tau_{osc}$ – oscilloscope time constant. Then the angular frequency $\omega_{-3\,dB}$ and frequency $f_c$ can be found from equations (19) and (20).

The measurement system with a spectrum analyzer is shown in Fig. 30. Measurements of the frequency characteristics should be made at constant radiation power and optimal value bias of the detector. In this setup, the signal from the analyzer is fed by a broadband amplifier to the radiation source. The modulated radiation emitted by the LED is focused on the detector area. The electrical signal from the detector output is amplified and then fed to the analyzer input. It follows from the spectrum analyzer principle that the voltage frequency at the beat frequency oscillator (BFO) output follows the frequency of the radiation source. This means that if the voltage frequency at the analyzer's input changes within the frequency of the detector operation, the voltage frequency at the BFO output automatically adjusts to these changes. The advantage of this system is the ease of measuring frequency characteristics.

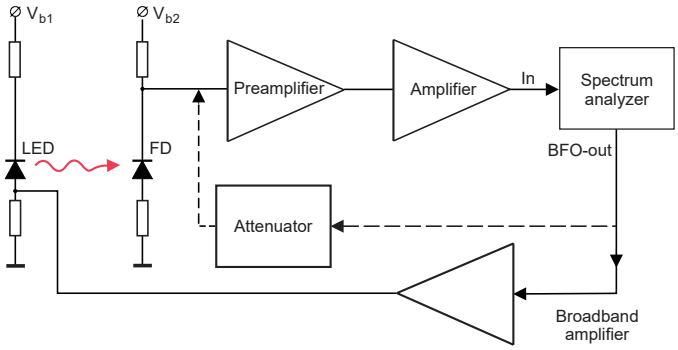


**Fig. 30.** Block diagram of the system used to measure frequency characteristics of the detectors

Moreover, the narrow bandwidth of the analyzer provides a high signal-to-noise ratio. Therefore, it is possible to use radiation sources with low output power. The disadvantage of the system is the narrow spectrum of the radiation source. The use of LEDs, e.g. GaAs or InAs, allows for obtaining radiation sources with wavelengths $\lambda$ of 0.8 and 3.2 μm, respectively.

To determine the frequency characteristics of the detector, the dependence of the output signal voltage on the modulation frequency $V_s(f)$ must be measured. After these measurements, the radiation source and a generator with an attenuator connected to the preamplifier should be switched off. Voltage $V_c$ indicated by the analyzer meter should be measured for the same frequencies.

The relative frequency response $w(f)$ of the detector shall be calculated from the equation below:

$$w(f) = \frac{V_s(f)V_c(f_o)}{V_c(f)V_s(f_o)}, \tag{51}$$

where $f_o$ is the frequency at which $w(f_o) = 1$.

In the heterodyne technique (Fig. 31), the registered signal is shaped by the profile of the output power line of the tuned laser. Spectra can be adjusted for the laser to give different frequencies, from 0 to those greater than 30 GHz. In the heterodyne setup, the laser beams of two lasers are combined. The optical signal with the "frequency-modulated sinusoidally at the difference" frequency is registered for the same polarization and amplitude of beams. This technique is characterized by a broad bandwidth limited by the tuning range of the laser (even 100 GHz or more). The modulated signal (photocurrent) is:

$$I_{ph(t)} = (P_{l1} + P_{l2})R(0) + 2\sqrt{P_{l1}P_{l2}}R(f)\cos(2\pi ft), \tag{52}$$

where $P_{lx}$ is the optical power delivered to the detector from the $x$-laser and $R(f)$ is the detector's responsivity at frequency $f$. The time-averaged photodetector current generated by the photodetector is then:

$$\begin{aligned} \langle I_{ph}^2 \rangle &= (P_{l1} + P_{l2})^2 R^2(0) + 2(P_{l1}P_{l2})R^2(f) \\ &= \langle I_{dc}^2 \rangle + \langle I_f^2 \rangle, \end{aligned} \tag{53}$$

where $I_{dc}$ is the DC photocurrent and $I_f$ is RF photocurrent flowing through a high-pass filter. The ratio of both currents defines relative frequency response determined as $R^2(f)/R^2(0)$. The frequency characteristics of this response ratio ensure the determination of detector bandwidth.

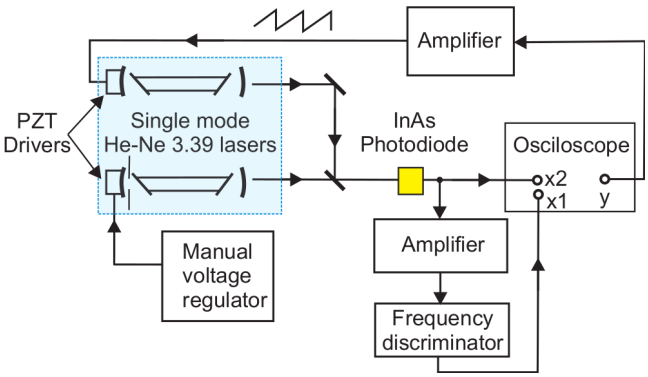


**Fig. 31.** Block diagram of photodetector frequency measurement [82]

Characteristics of some methods applied to frequency response measurement of the photodetector are described in Table 5.

**Table 5**
Characteristics of some measurement systems for photodetector frequency response

| | Method | Source | Wavelength | Type of excitation | Measured bandwidth | Ref. |
|---|---|---|---|---|---|---|
| 1 | Time response analysis | Ti:sapphire laser | 800 nm | laser pulse | 50 GHz | [83] |
| 2 | Heterodyne | DFB laser diode | 1 300 nm | thermal laser tuning spectra | 20 GHz | [84] |
| 3 | Pulse spectrum analysis | DFB laser | 1 300 nm | laser pulse | 16 GHz | |
| 4 | Heterodyne | Nd:YAG | 1 319 nm | thermal laser tuning spectra | 26.49 GHz | [85] |
| 5 | Two-tone optical method | DFB laser diode | 1 550 nm | microwave intensity-modulated | 12 GHz | [86] |
| 6 | Photocurrent shot-noise spectrum | DFB laser diode | 1 550 nm | noise signal | 164 MHz | [87] |
| 7 | White optical noise | superluminescent light-emitting diode | 1 550 nm | spontaneous-spontaneous heat noise | > 15 GHz | [88] |

Knowing the frequency characteristics of the detector voltage and noise current density, the frequency characteristics of the noise equivalent power density can be determined (Fig. 32).

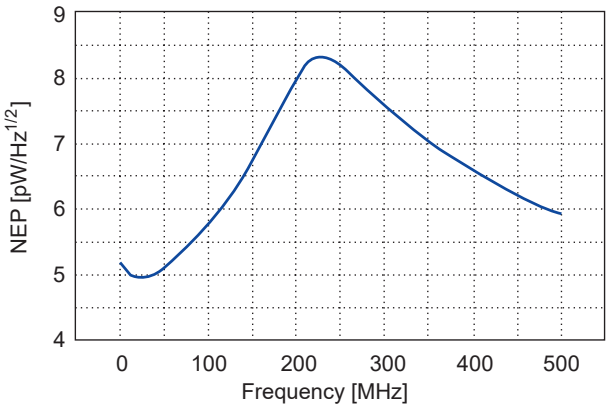


**Fig. 32.** NEP spectral characteristics of $p-i-n$ InGaAs photodiodes PDB460C type by Thorlabs [89]

For this purpose, noise current spectral density should be divided by the maximum value of the current responsivity $R_{i\max}(\lambda)$ of the detector under test (as NEP is usually given for $R_{i\max}$):

$$\mathrm{NEP}_{\min}(f) = \frac{I_{\mathrm{nd}}(f)}{R_{i\max}}. \tag{54}$$

Then, using the spectral responsivity characteristics of the detector $R_i(\lambda)$, the NEP frequency characteristics can be determined from the following equation:

$$\mathrm{NEP}(f) = \mathrm{NEP}_{\min}(f)\frac{R_{i\max}}{R_i(\lambda)}. \tag{55}$$

Knowing this characteristic (for any frequency range) can determine the minimum $P_{\min}$ power that a given detector can detect:

$$P_{\min} = \int_{f_l}^{f_u} \mathrm{NEP}(f)\,\mathrm{d}f. \tag{56}$$

### 3.6. Measuring method of directional characteristics

Directional characteristics are obtained by rotating the photodetector around the top of its lens (Fig. 33). They are usually expressed relative to a value of 1 for the angle with the highest output intensity.

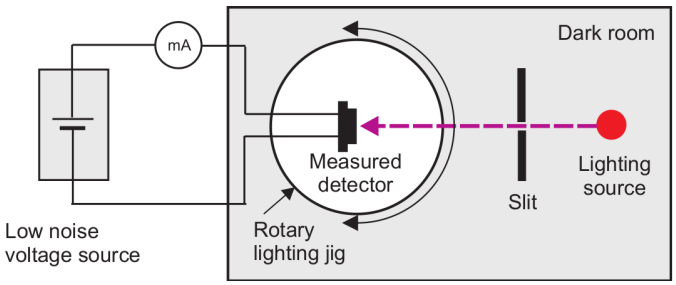


**Fig. 33.** Measuring method of directional characteristics

## 4. CONCLUSIONS

The article discusses some metrological aspects related to technology development and the application of photodetectors. It results from analyses and research conducted in order to standardize the concepts and measurement procedures associated with detector parameters. The most commonly used semiconductor detectors are described, with particular attention being paid to their internal structure, significantly impacting their performance and application. Some specific features of detectors at the stage of their design and production have also been described. Devices of this type are used in everyday life (e.g. in smartphones or smartwatches), in the industry (e.g. for product quality and composition control, in gas sensors), and in scientific research concerning *inter alia* space (e.g. for data transmission, measuring the composition of the Martian atmosphere). The last part of the article focuses on measuring those parameters that are most often analyzed by end-users. Theoretical models and equivalent diagrams are given, which constitute the basis for analyzing measurement results, measurement systems and their exemplary parameters.

## ACKNOWLEDGMENTS

The article was supported by a project entitled "Development of structure technology for single-mode cascade lasers for applications in optical gas detection systems" (ID: 347510) No. TECHMATSTRATEG1/ 347510/15/NCBR/2018.

We would like to thank Professor Józef Piotrowski for expert discussions and his many valuable comments.

## REFERENCES

[1] M.A. Kinch, "State-of-the-Art Infrared Detector Technology," *SPIE Press*, Bellingham, Washington, 2014, doi: 10.1117/3.1002 766.

[2] A. Rogalski, *Infrared and Terahertz Detectors*, 3nd edition, CRC Press, Boca Raton, 2019.

[3] D.E. Sidor, G.R. Savich, G.W. Wicks, "Surface Leakage Mechanism in III-V Infrared Barrier Detectors," *J. Electron. Mater.*, vol. 45, no. 9, pp. 4663–4667, 2016, doi: 10.1007/s11664-016-4451-3.

[4] J.D. Vincent, S. Hodges, J. Vampola, M. Stegall, and G. Pierce, *Fundamentals of Infrared and Visible Detector Operation and Testing*, 2nd edition, Wiley, New Jersey, 2016.

[5] W.L. Eisenman, J.D. Merriam, and R.F. Potter, "Operational characteristics of infrared photodetectors," in *Semiconductors and Semimetals*, vol. 12, R.K. Willardson and A.C. Beer, Eds. Academic Press, New York, 1977, pp. 1–37.

[6] J. Piotrowski and A. Rogalski, *High-Operating-Temperature Infrared Photodetectors*, SPIE Press, Bellingham, 2007.

[7] F.H.L. Koppens, T. Mueller, P. Avouris, A.C. Ferrari, M.S. Vitiello, and M. Polini, "Photodetectors based on graphene, other two-dimensional materials and hybrid systems," *Nat. Nanotechnol.*, vol. 9, pp. 780–793, 2014.

[8] W. Van Roosbroeck and W. Shockley, "Photon-radiative recombination of electrons and holes in germanium," *Phys. Rev.*, vol. 94, pp. 1558–1560, 1954.

[9] A.R. Beattie and P.T. Landsberg, "Auger effect in semiconductors," *Proc. R. Soc. Lond.*, vol. A 249, pp. 16–28, 1958.

[10] W. Shockley and W.T. Read, "Statistics of recombinations of holes and electrons," *Phys. Rev.*, vol. 87, pp. 835–842, 1952.

[11] R.N. Hall, "Electron-Hole Recombination in Germanium," *Phys. Rev.*, vol. 87, 387, 1952.

[12] J. Piotrowski and W. Gawron, "Ultimate performance of infrared photodetectors and figure of merit of detector material," *Infrared Phys. Techol.*, vol. 38, pp. 63–68, 1997.

[13] S.M. Sze, *Semiconductor Devices: Physics and Technology*, 3rd ed., Willey, 2012.

[14] S. Donati, *Photodetectors. Devices, Circuits, and Applications*. Prentice Hall PTR, New Jersey, 2000.

[15] T.J. Philips and N.T. Gordon, "Negative diffusion capacitance in Auger-suppressed HgCdTe heterostructure diodes," *J. Electron. Mater.*, vol. 25, no. 8, pp. 1151–1156, 1986.

[16] T. Markvart and L. Castaner, *Practical Handbook of Photovoltaics: Fundamentals and Applications*, Elsevier, Oxford, 2003.

[17] R.C. Jones, "Performance of detectors for visible and infrared radiation," in *Advances in Electronics*, vol. 5, L. Morton, Ed. Academic Press, New York 1952, pp. 27–30.

[18] A. Rogalski, "Progress in focal plane array technologies," *Prog. Quantum Electron.*, vol. 36, pp. 342–473, 2012.

[19] R.D. Hudson, *Infrared System Engineering*, Wiley, New York, 1969.

[20] "Photodiode Saturation and Noise Floor," *Thorlabs*. [Online]. Available: https://www.thorlabs.com/images/TabImages/Photodetector_Lab.pdf. [Accessed: 10 Dec. 2021].

[21] Vishay. *Measurement Techniques*. Document Number: 80085. 2012.

[22] A. Rogalski and Z. Bielecki, *Detection of optical radiation.* Taylor & Francis Group (in press).

[23] Keysight Technologies, Photodiode Test Using the Keysight B2980A Series B2981A/83A Femto/Picoammeter B2985A/87A Electrometer/High Resistance Meter. Technical Overview, 2015.

[24] Keysight Technologies, *Impedance Measurement Handbook a guide to measurement technology and techniques*, 2009.

[25] P.R. Thomson and T.C. Larson. "Method of measuring shunt resistance in photodiodes," *Measurement Science Conference*, Ancheim, 2001.

[26] T. Markvart and L. Castaner, *Solar Cells: Materials, Manufacture and Operation*, Elsevier, Oxford, 2004.

[27] T.F. Refaat and D.G. Johnson, "Absolute linearity measurement of photodetectors using sinusoidal modulated radiation," *Applied Optics*, vol. 51, no. 19, pp. 4420–4429, 2012.

[28] J.E. Martin, N.P. Fox, and P.J. Key, "A cryogenic radiometer for absolute radiometric measurements," *Metrologia*, vol. 21, p. 147, 1985.

[29] R.M. Liberati, A. Del Paggio, and M. Rossi, "Photodetector Spectral Response Estimation Using Black Body Radiation," *Physics*, vol. 1, pp. 360–374, 2019, doi: 10.3390/physics1030026.

[30] R.L. Richardson, H. Yang, and P.R. Griffiths, "Evaluation of a correction for photometric errors in FT-IR spectrometry introduced by a nonlinear detector response," *Appl. Spectrosc.*, vol. 52, pp. 565–571, 1998.

[31] R.O. Carter, N.E. Lindsay, and D.A. Beduhn, "Solution to baseline uncertainty due to MCT detector nonlinearity in FT-IR," *Appl. Spectrosc.*, vol. 44, pp. 1147–1151, 1990.

[32] K. Maham, A. Vaskuri, F. Manoocheri, and E. Ikonen, "Calibration of Near-Infrared Detectors Using a Wavelength Tunable Light Source," *Opt. Rev.*, vol. 27, pp. 183–189, 2020, doi: 10.1007/s10043-020-00586-9.

[33] T. Pohl *et al.*, "Absolute calibration of the spectral responsivity of thermal detectors in the near-infrared (NIR) and mid-infrared (MIR) regions by using blackbody radiation," *J. Sensors Sens. Syst.*, vol. 10, pp. 109–119, 2021 doi: 10.5194/jsss-10-109-2021.

[34] T. Pohl, P. Meindl, U. Johannsen, D. Taubert, and L. Werner, "Measurement of the absolute spectral responsivity in the mid-infrared based on the cryogenic electrical substitution radiometer and an optimized thermopile detector," *J. Sensors Sens. Syst.*, vol. 8, pp. 195–205, 2019, doi: 10.5194/jsss-8-195-2019.

[35] T. Varpula, H. Seppa, J.M., "SaariOptical power calibrator based on a stabilized green He–Ne laser and a cryogenic absolute radiometer," *IEEE Trans. Instrum. Meas.*, vol. 38, pp. 558–564, 1989.

[36] V.E. Anderson, N.P. Fox, and D.H. Nettleton, "Highly stable, monochromatic and tunable optical radiation source and its application to high accuracy spectrophotometry," *Appl. Opt.*, vol. 31, pp. 536–545, 1992.

[37] T.R. Gentile, J.M. Houston, and C.L. Cromer, "Realization of a scale of absolute spectral response using the National Institute of Standards and Technology high-accuracy cryogenic radiometer," *Appl. Opt.*, vol. 35, pp. 4392–4403, 1996.

[38] H. Rabus, F. Scholze, R. Thornagel, and G. Ulm, "Detector calibration at the PTB radiometry laboratory at BESSY," *Nucl. Instrum. Methods Phys. Res. Sect. A-Accel. Spectrom. Dect. Assoc. Equip.*, vol. 377, pp. 209–216, 1996

[39] L.A. Faria, L.F.M. Nohra, N.A.S. Gomes, and F.D.P. Alves, "A high-performance Test-Bed Dedicated for Responsivity Measurements of Infrared Photodetectors in a Wide Band of Low Temperatures," *Int. J. Optoelectron. Eng.*, vol. 2, pp. 12–17, 2012 doi: 10.5923/j.ijoe.20120203.01.

[40] O. Gravrand, J. Wlassow, and L. Bonnefond, "A calibration method for the measurement of IR detector spectral responses using a FTIR spectrometer equipped with a DTGS reference cell," *Proc. SPIE*, vol. 9154, p. 91542O, 2014

[41] W. Liu *et al.*, "Mid-infrared spectral responsivity scale based on an absolute cryogenic radiometer and a tunable quantum cascade laser," *Metrologia*, vol. 58, p. 025003, 2021, doi: 10.1088/1681-7575/abe02d.

[42] J. Zeng, G.P. Eppeldauer, L.M. Hanssen, and V.B. Podobedov, "Spectral responsivity calibrations of two types of pyroelectric radiometers using three different methods," *Proc. SPIE*, vol. 8355, p. 835503, 2012.

[43] Ł. Ciura, A. Kolek, D. Smoczyń, and A. Jasik, "Four-point probe resistivity noise measurements of GaSb layers," *Bull. Polish Acad. Sci. Tech. Sci*., vol. 68 pp. 135–140, 2020, doi: 10.24425/bpasts.2020.131839.

[44] K. Jaworowicz, C. Cervera, J. B. Rodriguez, and P. Christol, "Noise Characterization of Midwave Infrared InAs / GaSb Superlattice pin Photodiode," *IEEE Photonics Technol. Lett.*, vol. 23, no. 4, pp. 242–244, 2011, doi: 10.1109/LPT.2010.2093877.

[45] J. Smulko, A. Azens, L.B. Kish, and C.G. Granqvist, "Low-frequency current noise in electrochromic devices," *Smart Mater. Struct*., vol. 17, pp. 1–5, 2008, doi: 10.1088/0964-1726/17/2/025005.

[46] A. Kwiatkowski, M. Gnyba, J. Smulko, and P. Wierzba, "Algorithms of chemicals detection using Raman spectra," *Metrol. Meas. Syst.*, vol. 17, pp. 549–560, 2010, doi: 10.2478/v10178-010-0045-1.

[47] C. Pace, C. Ciofi, and F. Crupi, "Very low-noise, high-accuracy programmable voltage reference," *IEEE Trans. Instrum. Meas.*, vol. 52, pp. 1251–1254, 2003.

[48] "Keysight B2961A/B2962A 6.5 Digit Low Noise Power Source," *Keysight Technologies*, 2019. [Online]. Available: https://www.keysight.com/us/en/assets/7018-03526/data-sheets/5991-0663.pdf. [Accessed: 12 Dec. 2021].

[49] "SIM928 – Rechargeable Isolated Voltage Source. Data Sheet," *Stanford Research Systems*. [Online]. Available: https://www.thinksrs.com/downloads/pdfs/manuals/SIM928m.pdf. [Accessed: 12 Dec. 2021].

[50] G. Scandurra, G. Giusi, and C. Ciofi, "A very low noise, high accuracy, programmable voltage source for low frequency noise measurements," *Rev. Sci. Instrum*., vol. 85, pp. 1–9, 2014

[51] V.E. Ivanov and E.U. Chye, "Simple programmable voltage reference for low frequency noise measurements," *J. Phys. Conf. Ser.*, vol. 1015, p. 052011, 2018.

[52] K. Achtenberg, J. Mikołajczyk, C. Ciofi, G. Scandurra, and Z. Bielecki, "Low-noise programmable voltage source," *Electronics*, vol. 9, p. 1245, 2018, doi: 10.3390/electronics9081245.

[53] D. Talukdar, R.K. Chakraborty, S. Bose, and K.K. Bardhan, "Low noise constant current source for bias dependent noise measurements, *Rev. Sci. Instrum*., vol. 82, 2011, doi: 10.1063/1.3509385.

[54] G. Scandurra, G. Cannatà, G. Giusi, and C. Ciofi, "Programmable, very low noise current source," *Rev. Sci. Instrum*., vol. 85, p. 125109, 2014. doi: 10.1063/1.4903355.

[55] C. Ciofi, R. Giannetti, V. Dattilo, and B. Neri, "Ultra Low-Noise Current Sources," *IEEE Trans. Instrum. Meas*., vol. 47, pp. 78–81, 1998.

[56] "Sub-femtoamp Remote SourceMeter® SMU Instrument," *Tektronix*. [Online]. Available: https://download.tek.com/datasheet/6430.pdf. [Accessed: 12 Dec. 2021].

[57] "200mA 2-Terminal Programmable Current Source," *Analog Devices*. [Online]. Available: https:// www. analog.com/ media/en/ technical- documentation/ data- sheets/ lt3092.pdf. [Accessed: 12 Dec. 2021].

[58] T. Costa, M.S. Piedade, and M. Santos, "An ultra-low noise current source for magnetoresistive biosensors biasing," *2012 IEEE Biomedical Circuits and Systems Conference (BioCAS)*, 2012, pp. 73–76. doi: 10.1109/BioCAS.2012.6418507.

[59] N. Jiang, "A Large Current Source with High Accuracy and Fast Settling," *Analog Devices*, pp. 52–55, 2018.

[60] "Low-Noise Voltage Preamplifier," *Stanford Research Systems*. [Online]. Available: https://www.thinksrs.com/products/sr560.htm. [Accessed: 12 Dec. 2021].

[61] "SR570 Low-Noise Current Preamplifier," *Stanford Research Systems*. [Online]. Available: https://www.thinksrs.com/downloads/pdfs/manuals/SR570m.pdf. [Accessed: 12 Dec. 2021].

[62] "Model 5113 Pre-Amplifier Instruction Manual," *Ameteksi*. [Online]. Available: https://www.ameteksi.com/-/media/ameteksi/download_links/documentations/5113/model_5113.pdf. [Accessed: 12 Dec. 2021].

[63] "Model 5182 Current Preamplifier," *Ameteksi*. [Online]. Available: https://www.ameteksi.com/-/media/ameteksi/download_links/documentations/supportcenter/signalrecovery/instruction_manuals/222514-a-mnl-d.pdf. [Accessed: 12 Dec. 2021].

[64] "Small Instrumentation Modules SIM910 and SIM911 – Low noise voltage preamplifiers," *Stanford Research Systems*. [Online]. Available: https://www.thinksrs.com/downloads/pdfs/catalog/SIM910911c.pdf. [Accessed: 12 Dec. 2021].

[65] "DLPCA-200 Variable Gain Low Noise Current Amplifier Datasheet," *Femto*. [Online]. Available: https://www.femto.de/images/pdf-dokumente/de-dlpca-200.pdf. [Accessed: 12 Dec. 2021].

[66] F.A. Levinzon, "Ultra-low-noise high-input impedance amplifier for low-frequency measurement applications," *IEEE Trans. Circuits Syst. I-Regul. Pap.*, vol. 55, pp. 1815–1822, 2008, doi: 10.1109/TCSI.2008.918213.

[67] G. Scandurra, G. Gusi, and C. Ciofi, "Single JFET Front-End Amplifier for Low Frequency Noise Measurements with Cross Correlation-Based Gain Calibration," *Electronics*, vol. 8, p. 1197, 2019, doi: 10.3390/electronics8101197.

[68] K. Achtenberg, J. Mikołajczyk, and Z. Bielecki, "FET input voltage amplifier for low frequency noise measurements," *Metrol. Meas. Syst*., vol. 27 pp. 531–540, 2020, doi: 10.24425/mms.2020.132785.

[69] K. Achtenberg, J. Mikołajczyk, C. Ciofi, G. Scandurra, K. Michalczewski, and Z. Bielecki, "Low-frequency noise measurements of IR photodetectors with voltage cross correlation system," *Measurement*, vol. 183, p. 109867, 2021, doi: 10.1016/j.measurement.2021.109867.

[70] L. Ciura, A. Kolek, K. Michalczewski, K. Hackiewicz, and P. Martyniuk, "1/f Noise in InAs/InAsSb Superlattice Photoconductors," *IEEE Trans. Electron Devices*, vol. 67, pp. 3205–3210, 2020, doi: 10.1109/TED.2020.2998449.

[71] R. Ćwirko, J. Ćwirko, and Z. Bielecki, "Measurement system testing the optical radiation detectors in a broad temperature range," *Metrol. Meas. Syst*., vol. 16, pp. 491–500, 2009.

[72] Ł. Ciura, A. Kolek, W. Gawron, A. Kowalewski, and D. Stanaszek, "Measurements of low frequency noise of infrared photodetectors with transimpedance detection system," *Metrol. Meas. Syst*., vol. 21 pp. 461–472, 2014, doi: 10.2478/mms-2014-0039.

[73] N. Dyakonova, S.A. Karandashev, M.E. Levinshtein, B.A. Matveev, and M.A. Remennyi, "Low frequency noise in reverse biased P- InAsSbP / n- InAs infrared photodiodes," *Semicond. Sci. Technol*., vol. 34, 2019.

[74] K. Jaworowicz, C. Cervera, J. B. Rodriguez, and P. Christol, "Noise Characterization of Midwave Infrared InAs / GaSb Superlattice pin Photodiode," *IEEE Photon. Technol. Lett*., vol. 23, pp. 242–244, 2011, doi: 10.1109/LPT.2010.2093877.

[75] R. Taalat, P. Christol, and J. Rodriguez, "Dark Current and Noise Measurements of an InAs/GaSb Superlattice Photodiode Operating in the Midwave Infrared Domain," *J. Electron. Mater*., vol. 41, pp. 2714–2718, 2012, doi: 10.1007/s11664-012-2035-4.

[76] D. Ramos *et al.*, "1/f Noise and Dark Current Correlation in Midwave InAs/GaSb Type-II Superlattice IR Detectors," *Phys. Status Solidi A-Appl. Mat.*, vol. 218, p. 2000557, 2021, doi: 10.1002/ pssa.202000557.

[77] Y. An, H. Rao, G. Bosman, and A. Ural, "Characterization of carbon nanotube film-silicon Schottky barrier photodetectors," *J. Vac. Sci. Technol. B*, vol. 30, p. 021805, 2012, doi: 10.1116/1.3690645.

[78] A. De Iacovo, C. Venettacci, L. Colace, L. Scopa, and S. Foglia, "Noise performance of PbS colloidal quantum dot photodetectors," *Appl. Phys. Lett.*, vol. 111, p. 211104, 2017, doi: 10.1063/1.5005805.

[79] P. Kostov, W. Gaberl, M. Hofbauer, and H. Zimmermann, "Low Frequency Noise in CMOS PNP PIN Phototransistors," *2013 22nd International Conference on Noise and Fluctuations (ICNF)*, 2013, pp. 1–4, doi: 10.1109/ICNF.2013.6578993.

[80] P.D. Hale and D.L. Franzen, "Accurate characterization of high-speed photodetectors," *Proc. SPIE*, vol. 2022, Photodetectors and Power Meters, pp. 218–227, 1993, doi: 10.1117/12.158578.

[81] X. Wu, J. Man, L. Xie, J. Liu, Y. Liu, and N. Zhu, "A new method for measuring the frequency response of broadband optoelectronic devices," *IEEE Photonics J*., vol. 4, no. 5, pp. 1679–1685, 2012.

[82] K.M. Abramski, "Frequency response of photodetector measurements employing heterodyne and interferometric techniques of detection," *Opt. Appl.*, vol. 13, no. 3, pp. 223–229, 1983.

[83] T.S. Clement, P.D. Hale, K.C. Coakley, and C.M. Wang, "Time-domain measurement of the frequency response of high-speed photoreceivers to 50 GHz," in *Tech. Dig., Symp. on Optical Fiber Meas.*, 2000, pp. 121–124.

[84] S. Kawanishi, A. Takada, and M. Saruwatari, "Wideband frequency-response measurement of optical receivers using optical heterodyne detection," *J. Lightwave Technol.*, vol. 7, pp. 92–98, 1989.

[85] P.D. Hale, C.M. Wang, R. Park, and W.Y. Lau, "A transfer standard for measuring photoreceiver frequency response," *J. Lightwave Technol.*, vol. 14, no. 11, pp. 2457–2466, 1996, doi: 10.1109/50.548142.

[86] H. Wang *et al.*, "Two-tone intensity-modulated optical stimulus for self-referencing microwave characterization of high-speed photodetectors." *Optics Communications*, vol. 373, pp. 110–113, 2016.

[87] "Measure detector response using shot-noise," *Koheron.* [Online]. Available: https://www.koheron.com/blog/2017/01/05/detector-response-shot-noise. [Accessed: 15 Dec. 2021].

[88] E. Eichen, J. Schlafer, W. Rideout, and J. McCabe, "Wide-bandwidth receiver photodetector frequency response measurements using amplified spontaneous emission from a semiconductor optical amplifier," *J. Lightwave Technol.*, vol. 8, pp. 912–916, 1990.

[89] V. Mackowiak, J. Peupelman, Y. Ma, and A. Gorges, "NEP-Noise equivalent power," *Thorlabs*. [Online]. Available: https://www.thorlabs.com/images/TabImages/Noise_Equivalent_Power_White_Paper.pdf. [Accessed: 15 Dec. 2021].